



**HAL**  
open science

## **Facies associations, detrital clay grain coats and mineralogical characterization of the Gironde estuary tidal bars: A modern analogue for deeply buried estuarine sandstone reservoirs**

Maxime Virolle, Hugues Féliès, Benjamin Brigaud, Raphaël Bourillot, Eric Portier, Patricia Patrier, Daniel Beaufort, Isabel Jalon-Rojas, Hervé Derriennic, Serge Miska

### ► **To cite this version:**

Maxime Virolle, Hugues Féliès, Benjamin Brigaud, Raphaël Bourillot, Eric Portier, et al.. Facies associations, detrital clay grain coats and mineralogical characterization of the Gironde estuary tidal bars: A modern analogue for deeply buried estuarine sandstone reservoirs. *Marine and Petroleum Geology*, 2020, 114, pp.104225 (IF 3,538). 10.1016/j.marpetgeo.2020.104225 . hal-02447126

**HAL Id: hal-02447126**

**<https://hal.science/hal-02447126>**

Submitted on 21 Jul 2022

**HAL** is a multi-disciplinary open access archive for the deposit and dissemination of scientific research documents, whether they are published or not. The documents may come from teaching and research institutions in France or abroad, or from public or private research centers.

L'archive ouverte pluridisciplinaire **HAL**, est destinée au dépôt et à la diffusion de documents scientifiques de niveau recherche, publiés ou non, émanant des établissements d'enseignement et de recherche français ou étrangers, des laboratoires publics ou privés.



Distributed under a Creative Commons Attribution - NonCommercial 4.0 International License

1 **Facies associations, detrital clay grain coats and mineralogical characterization of the**  
2 **Gironde estuary tidal bars. A modern analogue for deeply buried estuarine sandstone**  
3 **reservoirs.**

4

5

6 Maxime Virolle<sup>1</sup>, Hugues Féniès<sup>2</sup>, Benjamin Brigaud<sup>1</sup>, Raphaël Bourillot<sup>2</sup>, Eric Portier<sup>3</sup>, Patricia  
7 Patrier<sup>4</sup>, Daniel Beaufort<sup>4</sup>, Isabel Jalon-Rojas<sup>5</sup>, Hervé Derriennic<sup>6</sup>, Serge Miska<sup>1</sup>

8

9 <sup>1</sup>Université Paris-Saclay, CNRS, GEOPS, 91405 Orsay, France

10 <sup>2</sup>Géoressources et Environnement, ENSEGID, Bordeaux INP, Université Bordeaux Montaigne  
11 33607 Pessac, France

12 <sup>3</sup>Neptune Energy, 9-11 Allée de l'Arche, 92400 Courbevoie, France

13 <sup>4</sup>Univ. Poitiers, IC2MP, CNRS, UMR 7285, TSA 51106 86073 Poitiers Cedex 9, France

14 <sup>5</sup>The Sino-Australian Research Centre for Coastal Management, School of Physical,  
15 Environmental and Mathematical Sciences, UNSW Canberra, Canberra, Australia

16 <sup>6</sup>EPOC-OASU, CNRS, Université de Bordeaux, Site de Talence, Bâtiment B18N, 33615 Pessac  
17 Cedex

18

19 Corresponding author: [maxime.virolle@u-psud.fr](mailto:maxime.virolle@u-psud.fr), GEOPS, Univ. Paris-Sud, CNRS, Université  
20 Paris-Saclay, 91405 Orsay, France

21

22 Short title: Multi-scale tidal bars characterization

23

## 24 Abstract

25

26 Estuarine tidal bar sandstones are complex reservoir geobodies commonly exploited by the  
27 oil and gas industry. In order to better predict the reservoir potential of these geobodies,  
28 this study provides a modern-day reservoir analogue, describing tidal bars in the inner and  
29 outer Gironde estuary from the microscopic to the macroscopic scale.

30 The originality of this work lies in the multi-scale study of modern estuarine tidal bars based  
31 on numerous piston cores extracted in a high-energy environment. This work demonstrates  
32 that these tidal bars are composite sedimentary bodies made up of individual reservoir sand  
33 units separated by thick muddy layers. Their vertical facies associations and internal  
34 architectures are controlled by local hydrodynamic variations and seasonal river influxes.  
35 Detrital clay grain coats are notably characterized using a portable and handheld mineral  
36 spectrometer from the base to the top of the tidal bars. X-ray diffraction and electron  
37 microscopes reveal that these coats are mainly composed of di-octahedral smectite, illite,  
38 chlorite and kaolinite associated with other components such as diatoms or pyrite. The best  
39 reservoir geobodies are those with the minimum clay permeability barriers at the macro and  
40 mesoscale. An optimum coated grain content and clay fraction volume is also needed for  
41 generating authigenic clay coatings and inhibiting quartz overgrowth. These conditions are  
42 met within the tidal sand bars of the outer estuary funnel that are expected to be the best  
43 reservoir geobodies in deeply buried sandstones.

44

45 Keywords: Tidal bars, hydrodynamic, coats, clay, reservoir.

46

## 47 1. Introduction

48

49 Estuarine sandstone geobodies are characterized by their internal architecture, which is  
50 highly variable and complex, both laterally and vertically (Olariu et al., 2012; Taylor et al.,  
51 2015). The successive deposition of clay-rich and sand-rich layers, as a consequence of  
52 temporal and spatial variations in tidal currents, influence their architecture (Reineck and  
53 Wunderlich, 1968; Visser, 1980; Dalrymple et al., 1991; Yoshida et al., 1999; Martinius et al.,  
54 2005; Massart, 2014). Tidal bars and heterolithic point bars deposited within estuaries  
55 display a multi-scale architecture and heterogeneity due to the succession of clay-rich and  
56 sand-rich layers (Féniès and Tastet, 1998; Tessier et al., 2012; Chaumillon et al., 2013;  
57 Shchepetkina et al., 2016). Within estuarine sandstones reservoirs, these heterogeneities  
58 will exert a key control on the flow of gas, oil and water during field production (Weber,  
59 1986; Jackson et al., 2005, 2003; Ringrose et al., 2005; Nordahl et al., 2005, 2006; Nordahl  
60 and Ringrose, 2008).

61 The aggregation of clay particles and sand grains generates micrometre scale (pore scale)  
62 heterogeneity within estuarine sand bars. Clay minerals may fill porosity but may also form  
63 coats around sand grains that will influence physical properties in buried sandstone  
64 reservoirs (Bloch et al., 2002; Wooldridge et al., 2017; Stricker and Jones, 2018). Previous  
65 studies showed that chlorite coatings may inhibit quartz overgrowth nucleation, one of the  
66 main porosity reduction mechanism, and thereby preserve reservoir quality at great depth  
67 (Ehrenberg, 1989; Houseknecht and Pittman, 1992; Bjorlykke and Egeberg, 1993; Ehrenberg,  
68 1993; Aase et al., 1996; Bloch et al., 2002; Storvoll et al., 2002; Bjørlykke, 2014). The  
69 formation of these coatings may originate from transformations of clay mineral precursors  
70 (e.g. berthierine or odinite; Worden and Morad, 2003; Gould et al., 2010; Beaufort et al.,

71 2015). Detrital clay grain coats formed within estuarine deposits can initiate chloritization by  
72 supplying the detrital material necessary to form the precursors (Beaufort et al., 2015;  
73 Griffiths et al., 2018, 2019a; Virolle et al., 2019). Exopolymeric substances (EPS) produced by  
74 diatoms may have a key role in binding clay particles around sand grains that are probably  
75 coated just before deposition within sand dunes (Jones, 2017; Virolle et al., 2019). Besides,  
76 primary depositional mineralogy (quartz, feldspars, carbonates and clay minerals)  
77 distribution also influence sandstone reservoir quality (Griffiths et al., 2019b). However,  
78 only few studies have analysed detrital clay grain coats and detrital minerals distribution in  
79 surface or sub-surface estuarine sediments (Shchepetkina et al., 2016; Wooldridge et al.,  
80 2017; Griffiths et al., 2018; Shchepetkina et al., 2018; Virolle et al., 2019). The Ravenglass  
81 Estuary, the Petitcodiac River, the Ogeechee River estuary and the Gironde are among the  
82 rare examples of high resolution study that investigate both surface and subsurface  
83 sediment in terms of clay coat, clay mineral and coarse-fraction mineralogy (Wooldridge et  
84 al., 2017; Griffiths et al., 2018, 2019a, 2019b).

85 Understanding the processes at the origin of multi-scale reservoir heterogeneities is a key  
86 scientific challenge for better predicting reservoir quality distribution at great depth. To do  
87 so, the best way remains studies of modern sedimentary analogues, of outcrops and of drill  
88 core (Wood, 2004; Musial et al., 2012; Olariu et al., 2012; Saïag et al., 2016; Aschoff et al.,  
89 2018)

90 In this study, we investigate tidal sand bars from the Gironde Estuary, which may be  
91 considered as a modern analogue of many ancient tidal bars (Allen, 1991). The Gironde  
92 estuary is a mud-rich, macrotidal estuary with heterolithic point bars and tidal bars up to  
93 several kilometres long, making them comparable in size to ancient estuarine reservoir  
94 geobodies, such as the Permian Cape Hay Formation (Bonaparte Basin, Australia; Saïag et al.,

95 2016), the Early Cretaceous Segó Formation (Colorado, United States; Aschoff et al., 2018) or  
96 the Cretaceous McMurray Formation (Alberta, Canada; Musial et al., 2012). Elongate tidal  
97 bars present both lateral and longitudinal accretion surfaces (Féniès and Tastet, 1998; Olariu  
98 et al., 2012; Chaumillon et al., 2013; Legler et al., 2013). The Gironde estuary is also  
99 characterized by a well-developed Turbidity Maximum Zone (TMZ), which allows the  
100 deposition of clay-rich layers within tidal bars (Allen, 1991; Féniès et al., 1999 ; Doxaran et  
101 al., 2009; Jalón-Rojas et al., 2015). Although many sedimentological studies have been  
102 carried out on the estuary, the relationship between hydrodynamics, vertical facies  
103 associations and the distribution of detrital clay grain coats and clay minerals remains poorly  
104 understood.

105 This paper presents the investigation of sediment cores drilled from two tidal bars located  
106 40 km apart in the Gironde estuary: the Plassac tidal bar, in the inner estuary funnel, and the  
107 Richard tidal bar, in the outer estuary funnel. Six 4.5 to 6.70 m long cores were extracted,  
108 three from each bar. Studies were conducted at the pore scale (micrometres), the facies  
109 association scale (metres), up to the reservoir architecture scale (hundreds of metres to  
110 several kilometres). Grain size, clay fraction content ( $< 2 \mu\text{m}$ ) and assemblage, coated grain  
111 abundance (percentage of grains with clay attached to their surfaces) and coat coverage  
112 were analysed from cores samples. A portable and handheld mineral spectrometer was used  
113 to test its robustness to characterize clays in sands. The facies and mineralogy described in  
114 this study may be useful for geologists describing detrital cores.

115 Specific research questions will be addressed:

- 116 • Do clay coats exist at several meters depth in modern tidal bars subjected to strong  
117 hydrodynamics? How are clay coats distributed in near surface estuarine sediments  
118 ( $<10\text{m}$ )? What processes controlled their formation and distribution?

119

- 120 • How are clay minerals distributed with depth and along the estuary?
- 121 • What are the processes governing the multi-scale heterogeneities within estuarine
- 122 tidal bars? Is that possible to predict which depositional environments will have the
- 123 best reservoir quality after burial?

## 124 2. [Study area: Gironde estuary](#)

125

### 126 2.1. [Morphological settings and studied sites](#)

127

128 The Gironde estuary is located in south-western France begins (Fig. 1). It is a worldwide  
129 reference model for mixed tide- and-wave-dominated incised valleys (Allen and  
130 Posamentier, 1994; Lericolais et al., 1998, Féniès et al., 2010). The estuary is divided into  
131 three morphological zones, comprising from upstream to downstream: (1) the Garonne and  
132 Dordogne estuarine meandering channels, characterized by the deposition of heterolithic  
133 point bars, (2) the inner estuary funnel, including the tidal bars of the bay-head delta, and (3)  
134 the outer estuary funnel, consisting in a wide muddy central basin with tidal bars and a large  
135 tidal inlet at its seaward extremity (Fig. 1: Allen, 1991 ; Virolle et al., 2019).

136 Two tidal bars have been studied in the Gironde during recent decades: (1) The Plassac tidal  
137 bar (Billy et al., 2012; Chaumillon et al., 2013), at the landward extremity of the bay-head  
138 delta, 65 km inland from the estuary mouth and (2) the Trompeloup tidal bar (Féniès et al.,  
139 1998), at the seaward extremity of the bay-head delta, 45 km inland from the estuary  
140 mouth. These tidal bars belong to the bay-head delta that extends from 75 to 35 km inland  
141 from the estuary mouth (Fig. 1). Fluvial sands deposited in the estuary funnel during the last

142 4000 years compose these tidal bars that are part of the Highstand Systems Tract (HST),  
143 which is gradually filling the Gironde Estuary funnel (Allen, 1991; Allen and Posamentier,  
144 1994).

145 This study focuses on two tidal bars located 40 km apart (Fig. 1): (1) the Plassac tidal bar,  
146 which is 4.6 km long and 1.4 km wide and located in the inner estuary funnel (described  
147 above), from which three new cores were collected and (2) the Richard tidal bar, in the outer  
148 estuary funnel, 25 km from the estuary mouth, from which another set of three cores was  
149 collected. This sandy tidal bar is about 4 km long and 300 m wide and has been deposited  
150 between tidal channels. Both tidal bars were chosen as they are well preserved, well-  
151 developed and remain accessible for coring.

152

## 153 2.2. Hydrodynamics of the Gironde estuary

154 In the Gironde, tides are semi-diurnal, and the estuary is macro-tidal (Allen, 1972). Tidal  
155 range between 2.5 and 5m on mean neap/spring tides at the estuary mouth (Bonneton et  
156 al., 2015). As tidal wave migrates upstream, both tidal amplitude and asymmetric shape of  
157 the wave are amplified (Jalon-Rojas et al., 2018). The Gironde estuary is therefore defined as  
158 a hypersynchronous estuary (Allen, 1991). At the upstream tidal current limit (160 km from  
159 the estuary mouth during the low-river stage), the tidal range and tidal-current velocities fall  
160 to zero (Allen, 1972; Allen et al., 1980).

161 For both tidal bars located in the estuary funnel, the ebb flow is the faster current (Allen,  
162 1972; Castaing, 1981; Féniès et al., 1999). For example, Féniès et al. (1999) measured  
163 maximum ebb velocity of  $80 \text{ cm}\cdot\text{s}^{-1}$  and maximum flood velocity of  $52 \text{ cm}\cdot\text{s}^{-1}$  during spring  
164 tides in the intertidal zone of the Plassac tidal bar. In the subtidal zone, tidal velocities can  
165 reach  $200 \text{ cm}\cdot\text{s}^{-1}$  and are still ebb dominated (Castaing, 1981).



166 The estuary is also characterized by a well-developed Turbidity Maximum Zone (TMZ) with  
167 Suspended Particle Matter (SPM) concentration that varies between 1-10 g.l-1 in the  
168 estuarine waters (Allen, 1972; Allen et al., 1977, 1980; Sottolichio et al., 2011; Savoye et al.,  
169 2012). This high turbidity zone has a major effect on sedimentation processes (Allen, 1972,  
170 Sottolichio et al., 2011). The TMZ position varies seasonally in the estuary with fluvial  
171 discharge (Allen, 1972).

172

### 173 [3. Material and methods](#)

#### 174 [3.1. Coring](#)

175 The originality of this study lies in the core dataset sampled from two tidal bars, the Plassac  
176 bar in the inner estuary and the Richard tidal bar in the outer estuary. Six campaigns were  
177 carried out to extract cores from the tidal bars. Three cores were sampled from each bar  
178 along East–West transects perpendicular to the long axis of the bars (North–South). On the  
179 Plassac tidal bar (45°06′24.49″N 0°39′37.87″W), the three campaigns took place on 23–26  
180 November 2015. Three cores, named PLA-2015-East, PLA-2015-Centre and PLA-2015-West  
181 were collected with a core spacing of about 150 m. The core lengths vary from 4.44 m to  
182 6.70 m. On the Richard tidal bar (45°26′19.18″N 0°54′37.81″W), the first core (Ri-2016-C)  
183 was extracted on 21 April 2016, and the other two on 19–20 October 2016 (Ri-2016-E and Ri-  
184 2016-W). Extraction was made along a 90 m long transect, with a core spacing of about  
185 45 m. The spacing is tighter than at Plassac because the Richard tidal bar is narrower. The  
186 core lengths vary from 4.60 m to 6.50 m.

187 Cores were recovered by using a portable vibro-corer (De Resseguier, 1983). During the  
188 coring process, the core barrel is hammed without any rotation and a reference line

189 indicating the ebb direction is marked all along the core section. At the lab, the core is open  
190 accordingly to this reference line, which allows distinguishing the orientation of the dune  
191 bedding (ebb & flood). The cores were opened and pictured at the “Sediment Archive  
192 Analysis” Platform at the EPOC laboratory (Univ. Bordeaux, France). Half of each core was  
193 used to describe sedimentary facies while the other half was used for sampling.

### 194 3.2. Petrography

195 Fifty-three plugs were sampled from the Plassac cores and 32 plugs from the Richard cores  
196 in a manner that prevented strong disturbance of the sedimentary fabric. Thin sections were  
197 made and observed in transmitted and reflected light.

198 As described in Virolle et al. (2019), the relative surface area (%) of the sediment  
199 components and the grain coat coverage were quantified. The macroporosity was  
200 determined by blue thresholding using Jmicrovision software. In each thin section, the  
201 relative surface area (%) of the coated and non-coated grains (quartz, feldspars, lithics,  
202 bioclasts, pyrite, micas) and also clay matrix were quantified using random grid point  
203 counting with JmicroVision Image analysis software (Roduit, 2007). Following the  
204 methodology described by Wooldridge et al. (2017a), the coated grains category was divided  
205 into four sub-categories depending on the grain coat coverage of the grain surface: (1) 1–5%,  
206 (2) 5–15%, (3) 15–30% and (4) more than 30%. Scanning Electron Microscope (SEM)  
207 observations were also realized on individual sand grains. Sediment grain size was analysed  
208 on 91 samples using a Mastersizer 2000 laser granulometer (Malvern, Worcestershire, UK).  
209 Mean grain size was calculated using Folk’s (1980) equation (see Virolle et al., 2019). During  
210 the experiment, mud pebbles were disaggregated and were therefore counted as a part of  
211 the fine fraction (<2 µm).

### 212 3.3. Mineralogy

213 As “clay” may refer to grain size as well as mineralogy, this study uses the term clay fraction  
214 to define the fine-grained fraction less than 2  $\mu\text{m}$  including clay minerals (Grim, 1942). The  
215 relative weight percentage of the clay fraction of homogenized sediment subsamples was  
216 measured and expressed as a weight percentage of the sample (wt. %; Virolle et al., 2019).  
217 The composition of the clay fraction ( $< 2 \mu\text{m}$ ) of 45 samples was determined by X-ray  
218 diffraction (XRD), and semi-quantitative estimations of clay mineral proportions were  
219 performed with Macdiff software. For analytical detail, see supplementary data S1.

220 Short wavelength infrared (SWIR) spectroscopy was performed on 391 samples using a  
221 portable and handheld spectrometer (ASDinc TerraSpec4 of PANanalytical): 162 samples  
222 from core PLA-2015-E, 175 samples from PLA-2015-W and 54 from Ri-2016-W. Mid-infrared  
223 (MIR) spectroscopy was performed on 10 samples from the Plassac tidal bar previously  
224 analysed by XRD. Sampling for SWIR was conducted every 2 cm. Analyses were conducted  
225 on bulk samples (any fraction combined, while only the fraction  $< 2 \mu\text{m}$  was studied in XRD).  
226 Cation exchange capacity (CEC) was measured on eight samples from PLA-2015-W. CEC was  
227 expressed in milli-equivalents per 100 g. CEC can be indicative of the proportion of  
228 “swelling” clays such as smectite in the sample. The detail of analytical procedure is available  
229 in supplementary data S1.

230 Three samples were also observed under Transmission Electron Microscopy (TEM), on a  
231 TECNAI G2 FEI TEM with an acceleration voltage of 200 kV and a spot size of about 5 nm.  
232 Most pictures were taken in TEM mode and analyses were performed in STEM (Scanning  
233 Transmission Electronic Microscopy) mode. The chemical composition obtained in oxide  
234 weight percentage (wt %) was converted into atomic percentage to estimate the structural

235 formulas. Then, calculated atomic concentrations were plotted in the ternary diagram M+4Si  
236 R2+ (Meunier and Velde, 1989) and used to determine intimate clay mixtures.

### 237 3.4. Datings

238 Large organic matter particles (wood fragments, leaves or seeds) were radiocarbon dated.  
239 For the Plassac tidal bar, the carbon 14 ( $^{14}\text{C}$ ) ages were obtained from the accelerator mass  
240 spectrometers (AMS) at the Adam Mickiewicz University in Poznań (Goslar et al., 2004) from  
241 14 samples. For the Richard tidal bar, the graphite sources were prepared at GEOPS (Univ.  
242 Paris-Sud, Orsay, France), and  $^{14}\text{C}$  counted with the low energy AMS "ECHO MICADAS -  
243 Environnement Climat et Homme Micro Carbon Dating System" at LSCE (Université Paris-  
244 Saclay/CEA/CNRS, Gif-sur-Yvette, France) on 29 samples. Analytical errors, including  
245 laboratory errors, are  $\pm 0.1\text{‰}$  for  $\delta^{13}\text{C}$  and between 0.5 and 0.8 pMC (percentage of Modern  
246 Carbon) for  $^{14}\text{C}$  activity. Gibert et al. (2002) provides a complete description of the  
247 equipment and protocol.

### 248 3.5. Hydrologic data

249 River discharge data monitored by the French Ministry of Ecology and Energy (Hydro  
250 database; <http://www.hydro.eaufrance.fr>) were used to determine seasonal estuary  
251 discharge. Estuary discharge is calculated as the sum of discharges from both the Garonne  
252 (monitored at Portet-sur-Garonne, upstream of the tidal influence, 43°31'15.39"N and  
253 1°24'8.71"E) and Dordogne (Cenac-et-Saint-Julien, 44°48'15.51"N and 1°12'22.74"E) from  
254 1925 to 1996 using annual mean values. Bathymetric data were obtained from the Bordeaux  
255 Harbour Authorities (Grand Port Maritime de Bordeaux).

256 Additional details concerning material and methods are provided in Appendix S1.

## 257 4. [Results](#)

258

### 259 4.1. [Facies characterization of the inner to outer estuary funnel tidal bars](#)

260 The facies descriptions are presented from the base to the top of the cores and are  
261 summarized in Table 1 and detailed grain composition in appendix S2. Globally, the vertical  
262 facies associations of both tidal bars present coarsening-upward grain-size trends: (i) for the  
263 Plassac bar, the average mean grain-size increases from 231  $\mu\text{m}$  at the base to 252  $\mu\text{m}$  at the  
264 top; (ii) for the Richard bar, it increases from 183  $\mu\text{m}$  (base) to 213  $\mu\text{m}$  (top). For both tidal  
265 bars, samples are composed of quartz (P= 31% and R= 27%), feldspars (P= 7% and R= 4%),  
266 lithics (P= 14% and R= 13%), carbonates (P= 3% and R= 6%), clay (P= 16% and R= 10%), pyrite  
267 (P= 0.24% and R= 0.5%), and others including micas or heavy minerals (P= 4% and R= 4%).  
268 The samples are classified into litharenite to feldspathic litharenite in the Folk diagram (Fig.  
269 2). Porosity values are higher in the Richard tidal bar (*ca.* 35%) than within the Plassac tidal  
270 bar samples (*ca.* 25%).

271 The bottom of both tidal bars is composed of the Fluid mud facies (F1). This facies is only  
272 observed on the Ri-2016-W core. In the Plassac tidal bar, it was observed in cores sampled in  
273 2010 (Chaumillon et al., 2013). Millimetre-thick stacked clay drapes, within which groups of  
274 sand ripples alternate with groups of linsens in a cyclic pattern, suggesting a neap-spring  
275 cycle layering, are observed in the Plassac tidal bar (F1a). In the Richard tidal bar, decimetre-  
276 thick homogeneous fluid mud layers composed this facies (F1b). Clay fraction within samples  
277 is about 29 wt% (Richard tidal bar, Table 2). Then, tidal bars are composed by the Lower  
278 sand bar facies (F2) whose main characteristics are small dunes with abundant centimetre-  
279 sized mud pebbles and numerous millimetre thick clay drapes deposited on the dune

280 foresets and bottomsets (Figs 3 and 4; Table 1). Clay drapes and mud pebbles are thicker and  
281 more abundant on the Plassac tidal bar. The clay fraction is about 21 wt% for Richard and 25  
282 wt% for Plassac (Table 2). Above, it is the Middle sand bar facies (F3) in the middle part of  
283 both tidal bars (Figs 3 and 4; Table 1). This facies is composed by small to medium-sized  
284 dunes with rare mud pebbles and thin clay drapes deposited on dune foresets and  
285 bottomsets (Figs 3 and 4; Table 1). The clay fraction is *ca.* 14 wt% for Richard and 15 wt% for  
286 Plassac (Table 2). Bioclast fragments and foraminifera are observed in thin sections. The  
287 middle part of both tidal bars is also composed by the Middle bar muddy facies (F4). In the  
288 Plassac tidal bar, it consists of a muddy matrix that exhibits characteristic lenticular bedding  
289 with millimetre-thick alternations of very fine-grained silty lenses and slack-water clay  
290 drapes (F4a; Fig. 3; Table 1). It was recovered in the Pla-2015-E core only. In the Richard tidal  
291 bar, this facies is observed in all three cores (F4b) and also exhibits the characteristic  
292 lenticular bedding described above (Fig. 4). The middle part of both tidal bars is covered by  
293 the Upper sand bar facies (F5; Figs 3 and 4). Sedimentary structures within both tidal bars  
294 are almost identical with small tidal dunes, but the difference is in the preserved clayey  
295 sedimentary structures: abundant centimetre-thick mud pebbles and thick clay drapes are  
296 deposited on dunes foresets and bottomsets within the Plassac tidal bar (F5a), while rare  
297 clay drapes and clay pebbles are deposited within the Richard tidal bar (F5b; Figs 3 and 4;  
298 Table 1). The clay fraction is *ca.* 20 wt% in (F5a) while it is *ca.* 17wt% in (F5b; Table 2). Facies  
299 (F5) is the last facies observed within the Richard tidal bar (Fig. 4). In the Plassac tidal bar,  
300 facies (F5) is capped by the Tidal flat facies (F6) made of flaser, wavy and lenticular bedding  
301 (Table 1). Finally, the Tidal marsh facies (F7) is the top of the vertical facies association of the  
302 Plassac tidal bar with amalgamated high-tide slack-water clay drapes, organic matter debris

303 and abundant reed roots (Fig. 3; Table 1). Top of the Plassac tidal bar (from F5 to F7) is  
304 therefore finning-upward.

305

#### 306 4.2. Tidal sand bar internal architecture

307

308 A reconstruction of the bars' internal architecture is proposed (Fig. 5 for the Plassac tidal  
309 bar, and Fig. 6 for the Richard tidal bar).

310 In the Plassac tidal bar (Fig. 5), the Lower sand bar facies (F2) is laterally continuous between  
311 the central and eastern cores (PLA 2015-C, PLA 2015-E), and the western core (PLA 2015-W)  
312 was probably not long enough to reach this facies. Above it, the Middle sand bar facies (F3)  
313 is a meter-thick laterally continuous layer, which constitutes the bulk of the tidal bar. This  
314 facies (F3) is capped by the Upper sand bar facies (F5a) that is also laterally continuous  
315 across the tidal bar. On the eastern part of the bar (core PLA 215-E) two layers of the F5a  
316 facies are isolated from one another by an eastward dipping layer of the Middle bar muddy  
317 facies (F4a). The (F5a) facies is capped by the Tidal flat facies (F6) as observed in the western  
318 and middle cores (PLA 2015-W, PLA 2015-C). It thickens westward and dips gently in the  
319 same direction. It is noteworthy that the major part of the tidal bar is composed of sandy  
320 units (facies F2, F3 and F5a) that are vertically and laterally connected to each other (Fig. 5)  
321 and could be considered as a single reservoir cell. The only reservoir heterogeneity is  
322 observed on the eastern side of the bar, where a decimetre-thick layer of the Middle bar  
323 muddy facies (F4a) isolates two metre-thick layers of the Upper sand bar facies (F5a).

324 The fourteen radiocarbon ages ( $^{14}\text{C}$ ), measured on the three cores (PLA 2015-W, PLA 2015-C,  
325 PLA 2015-E) show very heterogeneous ages, ranging from 5230  $\pm$ 40 years Before Present  
326 (BP) to the present. Except for one age (5230  $\pm$ 40 years BP), all  $^{14}\text{C}$  ages are younger than

327 1,000 years BP (Fig. 5). Modern ages and younger than 200 years BP are dominant in the  
328 upper part of the tidal bar (Facies F5 and F6, Fig. 6).

329 In the Richard tidal bar (Fig. 6), the Fluid mud facies (F1b) was encountered at the base of  
330 the bar in two cores (Ri-2016 W and Ri-2016-E). The central core (Ri-2016-C) was not long  
331 enough to reach this facies. Then, the Lower sand bar facies (F2) and the Middle bar facies  
332 (F3) are laterally continuous and thicken westward (Fig. 6). The Middle bar muddy facies  
333 (F4b), which caps the (F3) facies, is laterally continuous across the tidal bar. It dips gently  
334 ( $1.5^\circ$  dip-angle) and thickens eastward. Then, the Upper sand bar facies (F5b) was deposited  
335 at the top of the tidal bar on the Middle bar muddy facies (F4b). It is laterally continuous  
336 across the bar and it thickens eastward like the Middle bar muddy facies (F4b). On the  
337 Richard tidal bar, the thickness of the groups of facies varies laterally. At the base of the bar,  
338 facies (F2) and (F3) thicken westward, while at the top of the bar facies (F4b) and (F5b)  
339 thicken eastward, suggesting that the bar was laterally accreting to the West during the  
340 deposition of facies (F2) and (F3), and to the East during the deposition of facies (F4b) and  
341 (F5b). The tidal bar is composed of sandy units (facies F2, F3 and F5a) that are vertically and  
342 laterally connected to each other (Fig. 5) and could be considered as one reservoir cell. The  
343 main reservoir heterogeneity of the Richard tidal bar is a decimetre-thick layer of Middle bar  
344 muddy facies (F4b) that completely isolates the lower part of the bar (facies F1b, F2, F3)  
345 from the upper part of the bar (facies F5b). Therefore, if the Middle bar muddy facies (F4b) is  
346 spatially continuous, the Richard tidal bar would be composed of two reservoir cells.

347 Six  $^{14}\text{C}$  datings sampled on the three cores (Ri-2016-W, Ri-2016-C, Ri-2016-E) show very  
348 heterogeneous ages, ranging from 1996 years BP to the present. Here again, in spite of the  
349 age uncertainties, the  $^{14}\text{C}$  ages indicate that the bar was deposited very recently: all but one



350 of the  $^{14}\text{C}$  ages are younger than 300 years BP. The oldest age ( $1\,996 \pm 25$  years BP) is located  
351 in the Fluid mud facies (Fig. 6).

352

### 353 4.3. Detrital clay grain coat characterization

354

355 Clay coats correspond to a three-dimensional, clay-dominated coat around sand grains,  
356 which partially or totally covers the surface of sand grains (Dowey et al., 2017). On both tidal  
357 bars, clay coats can be observed on various framework grains (quartz, micas, feldspars,  
358 lithics), in each facies composing the tidal bars, down to a depth of almost 7 m below the  
359 surface of the bar (Figs 7 to 10). Main components are clay minerals, associated with other  
360 elements such as pyrite, diatoms, coccoliths or silt-sized quartz (Figs 7A-I and 8A-I). Diatom  
361 frustules can be observed down to the base of the cores (Figs 7F, 7I, 8E and 8I). Carbonated  
362 components (e.g. coccoliths) are more abundant in the Richard tidal bar in the outer estuary  
363 funnel (Fig. 8A and 8B). In this tidal bar, coats are also observed around bioclasts (e.g.  
364 holoturian spicules; Fig. 8A and 8B). Within both tidal bars, framboidal pyrite can be  
365 observed embedded within detrital clay grain coats (Figs 7C-D and 8C and 8D). Pyrite seems  
366 more abundant in the Richard tidal bar clay coats than in the Plassac tidal bar, but remains  
367 marginal compared to other components (average of 0.5% and 0.2% of total sample volume  
368 at Richard and Plassac, respectively).

369 As observed in the intertidal zone, detrital clay grain coats display various textures (Virolle et  
370 al., 2019). The commonest coat textures at Plassac are: 1) partial clay drapes, partly covering  
371 the surface of detrital grains, 2) aggregated detrital clay grain coats, scattered on the surface  
372 of sand grains and 3) bridged detrital clay grain coats, connecting detrital grains together

373 (Fig. 7 A-G). Aggregated clay coats are the commonest textures within the Richard tidal bar  
374 (Fig. 8A-G).

375 Within the Plassac tidal bar, detrital sand grains account for 59% of the total sample volume  
376 on average, and among this percentage, 22% of sand grains are coated (Table 2 and  
377 appendix S2). The abundance and distribution of coated grains associated with coat  
378 coverage classes are presented in Figure 9. On average, 6% of grains are coated by clays  
379 covering 15–30% of the grain surface (Fig. 9, Table 2). For each core from the Plassac tidal  
380 bar, detrital clay grain coats can be observed from the top to the base, down to a depth of  
381 6.65 m (depth of the last sample in the deepest core, the PLA-2015-C; Fig. 9). For all the  
382 facies and cores gathered on the Plassac tidal bar, coated grain content is not correlated  
383 with depth, mean grain size or porosity variations.

384 Figure 10 shows the coated grain content evolution with associated coat coverage classes  
385 within the Richard tidal bar. Detrital clay grain coats can be observed from the top to the  
386 bottom of cores, down to a depth of 6.40 m (depth of the last sample in the deepest core,  
387 the Ri-2016-W; Fig. 10). Detrital sand grains represent on average 55% of the samples,  
388 including 13% of coated grains (Table 2). Only 3% of coated grains have a coat coverage of  
389 15–30% of grain surfaces (Table 2). Considering all facies and cores from the Richard tidal  
390 bar, coated grain content is not correlated with depth, mean grain size or porosity  
391 variations.

392 Coated grain content is roughly constant along the vertical facies association of both tidal  
393 bars (Fig. 11, Table 2). For the Plassac tidal bar, the coated grain content is slightly higher in  
394 the sandiest facies (F2, F3 and F5a at 21%, 23% and 24%, respectively) and its proportion  
395 slightly decreases in muddy facies (F6 with 19%; Table 2). For the Richard tidal bar, coated  
396 grain content is comparatively steady, ranging from 11% to 17% (Table 2). Taking into

397 account all cores, the commonest coat coverage class for both tidal bars is 5–15% (7% of  
398 coated grains for Plassac, 5% for Richard; Table 2).

399

#### 400 4.4. Clay fraction and clay assemblages

401

402 For each tidal bar, the clay assemblage is composed of four clay minerals determined by XRD  
403 analysis (Fig. 12A-B): (i) chlorite, characterized by a (001) diffraction peak at 14.10 Å, (002) at  
404 7.05 Å, (003) at 4.73 Å and (004) at 3.54 Å; (ii) illite diffraction patterns show a (001)  
405 diffraction peak around 9.99 Å, (002) at 4.99 Å and (003) at 3.33 Å; (iii) kaolinite displays a  
406 (001) diffraction peak at 7.16 Å, and a (002) diffraction peak at 3.57 Å; and (iv) smectite is  
407 identifiable after ethylene-glycol saturation, with a (001) diffraction peak close to 17 Å.

408 The clay fraction content is mostly located within muddy deposits (e.g. fluid mud layers, clay  
409 drapes or mud pebbles) and sand coats within samples. All samples taken together, the clay  
410 fraction content is on average *ca.* 24 wt% within the Richard tidal bar and *ca.* 30 wt% within  
411 the Plassac tidal bar (Table 2). For the Plassac tidal bar, the clay fraction is almost constant  
412 between cores, ranging from 21 wt% in PLA-2015-C to 25 wt% in PLA-2015-W (Fig. 9). There  
413 is no correlation between the clay fraction content and the porosity or the coated grain  
414 content variations in this tidal bar. For the Richard tidal bar, clay content decreases slightly  
415 towards the middle of the bar: it is *ca.* 22 wt % on Ri-2016-W, 19 wt % on Ri-2016-E and 17  
416 wt % on Ri-2016-C (Fig. 10). Globally, there is no correlation between clay fraction content  
417 and coated grain content or porosity variations.

418 The clay fraction content varies between each facies. The results are presented in Table 2  
419 and Figs 9 and 10. Mud rich facies display the highest clay fraction content (F1b, F4a, F4b  
420 and F6 with respectively 29 wt%, 58 wt%, 37 wt% and 34 wt%). In the sandy facies, the clay

421 fraction ranges between 14 wt% and 25 wt%. The clay fraction within F1b might be  
422 underestimated because, in order to study coasts, sandy ripples were oversampled compared  
423 to muddy intervals in this facies.

424 Within the Plassac tidal bar, semi-quantitative analyses of XRD diffractograms show that the  
425 clay fraction is, on average, mostly composed of smectite and illite (peak surface areas of  
426 14% and 11%, respectively) with lower proportions of chlorite and kaolinite (Fig. 12A, Table  
427 2). Clay assemblages are similar in the different cores (Fig. 9). Semi-quantitative analysis on  
428 XRD diffractograms from the Richard tidal bar clay fraction indicate that it is composed of  
429 illite, smectite, kaolinite and chlorite, with surface areas ranging on average from 16% (illite)  
430 to 2% (chlorite) of the clay fraction (Fig. 12B, Table 2).

431 FTIR measurements were made along each core from Plassac, and only on core Ri-2016-W  
432 from Richard (Figs 9, 10 and 12C). All the spectra obtained are similar, showing that the clay  
433 assemblage is constant overall between vertical facies associations (Fig. 12C). But a focus on  
434 specific adsorption bands, such as the water band (1900 nm) or the bands characteristic of  
435 aluminous phases (at 2200 and 2253 nm) reveals local variations (Figs 9 and 10). For the  
436 Plassac tidal bar, the water band tends to increase near the surface, especially on core PLA-  
437 2015-C (Fig. 9). It can be correlated with an increase in the contribution from swelling clay  
438 minerals, such as smectite, upwards in this core. The bands at 2200 nm ( $\text{Al}_2\text{OH}$ ) and 2253  
439 nm, both mainly characterizing aluminous phases such as micas or clay minerals, do not  
440 show detectable variations with depth (Fig. 9). In the Ri-2016-W core, a slight increase in  
441 each band is observed, showing an increase in the smectite contribution and in aluminous  
442 phases with depth (Fig. 10).

443 TEM analyses were made on isolated particles from suspended material and plotted in a  
444 ternary diagram in the  $\text{M}^+ \text{-}4\text{Si-R}^{2+}$  system (Fig. 12D). The two plotted samples (6O and 22D,

445 respectively at 275 cm and 650 cm from the top of core PLA-2015-C) are representative of  
446 the other samples and are consistent with XRD and FTIR results. This confirms that most clay  
447 minerals belong to the families of smectite, illite and kaolinite, and that most of the particles  
448 have intermediate compositions such as those obtained through weathering processes  
449 confirming their detrital origin (Fig. 12D). Smectite is probably in a dioctahedral form, similar  
450 to montmorillonite (Fig. 12D).

451

## 452 [5. Discussion](#)

453

### 454 [5.1. Relation between vertical facies associations, tidal bar internal architecture](#) 455 [and hydrodynamic conditions](#)

#### 456 [5.1.1. Turbidity and tidal current velocity control on tidal bar vertical facies associations](#)

457

458 Vertical facies associations (Figs 3 and 4) observed within both tidal bars result from specific  
459 hydrodynamic processes. A coarsening-upward pattern is observed in the lower two-thirds  
460 of the bars, which is due to a thickening-upward trend of sand bed thicknesses, from the  
461 lower subtidal zone at the base of the bar (facies F1: Fluid mud facies, facies F2: Lower sand  
462 bar facies), to the upper subtidal zone (facies F3: Middle sand bar facies). They are also  
463 characterized by a fining-upward pattern, identified in the upper third of the bar, due to a  
464 thinning-upward trend of sand bed thicknesses. It is observed from the base of intertidal  
465 zone (facies F5: Upper sand bar facies) to the top of the intertidal zone (facies F6 and F7:  
466 Tidal flat and Tidal marsh facies).

467 Two hydrodynamic processes may explain these coarsening- and fining-upward patterns.  
468 The coarsening-upward pattern, described in the subtidal part of the tidal bars may be  
469 explained by the presence of a metre-thick fluid mud layer located at the bottom of the  
470 estuary funnel, at the base of the tidal bars.

471 The Fluid mud facies (F1, Figs 3 and 4) is deposited at the base of tidal bars within the FMZ  
472 that seasonally migrates with fluvial discharges variations (Fig. 13A-B). This FMZ is  
473 characterized by a very high SPM concentration ( $100\text{--}300\text{ g.l}^{-1}$ ) and a high viscosity, which  
474 slows the tidal current velocity to below the dune migration threshold. The tidal current  
475 velocity exceeds the ripple migration threshold only.

476 The Lower sand bar facies (F2, Figs 3 and 4) is deposited above the FMZ, within less turbid  
477 and less viscous waters (Fig. 13 A). Consequently, the current velocity increases above the  
478 dune migration threshold and the bed thickness increases up to that of small dunes.

479 The Middle sand bar facies (F3, Figs 3 and 4) is deposited in major part of the subtidal zone,  
480 up to the low tide limit, in waters with a low SPM concentration ( $1\text{--}3\text{ g.l}^{-1}$ ). The decreasing  
481 turbidity and viscosity of the water column allows an increase in the tidal current velocity  
482 and the bed thickness increases up to that of medium-size dunes.

483

484 The fining-upward pattern, observed from the base to the top of the intertidal zone, from  
485 facies F5: Upper sand bar facies, to facies F6 and F7: Tidal flat facies and Tidal marsh facies,  
486 may be explained by a tidal current velocity model presented in Fig. 13 C. It shows that in  
487 the intertidal shallow waters, the velocity of the tidal flows is reduced because the friction  
488 coefficient increases due to the reduction in the water column depth. This explains why the  
489 dunes are smaller in the Upper sand bar facies (F5) than in the subtidal Middle sand bar

490 facies (F3), and why the current velocity falls below the dune migration threshold in the Tidal  
491 flat facies (F6) and below the ripple migration threshold in Tidal marsh facies (F7).

492

#### 493 5.1.2. Short term climatic cycles control on tidal bar internal architecture

494

495 In the Gironde estuary, the extensive bathymetric map dataset compiled by the Bordeaux  
496 Harbour Authorities (Grand Port Maritime de Bordeaux) since the beginning of the twentieth  
497 century enabled the reconstruction of the morphological evolution of the inner estuary tidal  
498 bars: Trompeloup (Féniès and Tastet, 1998) and Plassac (Billy et al., 2012; Chaumillon et al.  
499 2013). Our study presents the morphological evolution and the internal architecture of an  
500 outer estuary tidal bar (Richard). New  $^{14}\text{C}$  ages from the cores of Plassac and Richard tidal  
501 bars also allow us to better time-constrain their internal architecture. Based on the papers  
502 publish on the Gironde estuary (Allen, 1991; Allen and Posamentier, 1994; Féniès and Tastet,  
503 1998; Chaumillon et al., 2013) and the use of maps of the Gironde estuary since the  
504 seventeen century (Gascuel, 2017), tidal bars are recent geobodies deposited during the last  
505 millennium.

506 For the Plassac tidal bar (Fig. 5), Carbon-14 ages exhibit very heterogeneous ages, ranging  
507 from 5,230 years BP to present. An age of  $75 \pm 30$  years BP at the top of the Lower sand bar  
508 facies (depth of 5.05 m) suggests that the Plassac tidal sand bar is relatively young, and was  
509 probably deposited during the last century. Older  $^{14}\text{C}$  ages suggest that old organic clasts  
510 could have been remobilized during recent episodes of accretion and erosion of the tidal  
511 bar. This age frame is consistent with the data published by Chaumillon et al. (2013) who  
512 demonstrate, based on the study of ancient bathymetric maps (Bordeaux Harbour  
513 Authorities), that most of the eastern spit of the Plassac tidal bar was deposited after 1908.

514 Billy et al. (2012) and Chaumillon et al. (2013) also demonstrate that the morphological  
515 evolution and internal architecture of the Plassac tidal bar are controlled by short term  
516 climatic cycles (Fig. 14A). During periods of high river discharge, the bar is laterally accreting  
517 and lateral accretion sand packages (LASP; named facies F1, F2, F3, F5a, in this study) are  
518 deposited. During periods of low river discharge, the lateral accretion process stops and a  
519 mud layer (named facies F4a, in this study) caps the previously deposited lateral accretion  
520 sand package.

521 On the Richard tidal bar (Fig. 6), in spite of age uncertainties, the  $^{14}\text{C}$  datings indicate that  
522 the bar has been deposited during the modern age: all but one of the  $^{14}\text{C}$  ages are younger  
523 than 300 years BP. An age of  $102 \pm 20$  years BP in the Middle sand bar facies indicates that  
524 the Richard tidal sand bar is relatively young, and was probably deposited during the last  
525 century. Here again, older  $^{14}\text{C}$  ages suggest that old organic clasts could have been  
526 remobilized. The historic bathymetric maps of the Bordeaux Harbour authorities show that  
527 the Richard tidal bar was mapped for the first time in 1901, which is consistent with our  
528 radiocarbon ages. The cores sampled in the Richard tidal bar, associated with the ancient  
529 bathymetric maps allow us to reconstruct its morphological evolution over time and to  
530 understand its internal architecture (Figs 6 and 14B). The bar is composed of two vertically  
531 stacked sand bodies, separated by a muddy layer.

532 According to the historical charts, the lower sand body (facies F1b, F2, F3) was deposited  
533 during the first half of the twentieth century, probably between 1900 and 1940. During this  
534 period, the bar was laterally accreting landward and its volume and length increased (from 3  
535 to 6 km long). Figure 6 shows a westward thickening of the lower sand body due to the  
536 landward migration of the bar. This period was characterized by relatively high river  
537 discharges (Fig. 15). Between 1940 and 1968, a decrease in the bar volume and length (from



538 6 to 2.5 km) is observed, correlated with the deposition of the muddy layer (facies F4b) at  
539 the top of the lower sand body (the  $^{14}\text{C}$  datings indicate put this muddy layer at  $71 \pm 20$  year  
540 BP, i.e. around  $1950 \pm 20$  - Fig. 6). At the beginning of this period, a decade of low river  
541 discharges was observed from 1942 to 1950 (Fig. 15). This low-river discharge period,  
542 associated with a lower sand supply, may have allowed the deposition of the muddy-layer  
543 (F4b). The lower sand body was probably abandoned and partially eroded before the  
544 deposition of the muddy layer. The upper sand body (facies F5b) was deposited between  
545 1968 and probably nowadays and covered the muddy layer (facies F4b). During this period,  
546 the bar was laterally accreting seaward (Fig.14B) and its volume and length increased (from  
547 2.5 to 7 km long). Figure 6 shows an eastward thickening of the upper sand body due to the  
548 seaward migration of the bar. This period is again characterized by relatively high river  
549 discharges (Fig. 15).

550 The internal architecture of the Richard tidal bar is very similar to that of the Trompeloup  
551 tidal bar, which is also made of two vertically stacked sand bodies, partially isolated from  
552 one another by a muddy layer (Féniès and Tastet, 1998).

553

## 554 5.2. Facies comparison of inner and outer tidal bars within the Gironde estuary

555

556 The Plassac tidal bar is located in the bay-head delta within the inner Gironde estuary 65 km  
557 inland from the estuary mouth, whereas the Richard tidal bar is located in the outer Gironde  
558 estuary, 25 km inland from the estuary mouth. In spite of their different locations within the  
559 estuary, the two tidal bars exhibit similar facies associations (Figs 5 and 6, Table 1). The Fluid  
560 mud facies (F1a and F1b) deposited at the base of the tidal bars shows only slight  
561 differences. Fluid mud facies F1a observed at the base of the Plassac tidal bar is composed of

562 numerous clay drapes stacked one upon the other with interbedded silt lenses and sand  
563 ripples. It is interpreted to be a high-energy fluid mud facies (Fig. 3). Similar observations  
564 were made within the Tilje Formation with fluid mud facies in tidal-fluvial channel deposits.  
565 Ichaso and Dalrymple (2009) showed that current-generated sedimentary structures  
566 produced by the migration ripples are present. Fluid mud facies F1b observed at the base of  
567 the Richard tidal bar looks visually more homogeneous than the F1a facies, but X-rays of the  
568 facies F1b allows to see that it is stratified. It consists of numerous clay drapes stacked one  
569 upon the other alternating with very thin silt lenses. The depositional processes of facies F1a  
570 and F1b are the same, and facies F1b is interpreted to be a low-energy fluid mud facies. This  
571 facies difference might be due to the fact that the Richard tidal bar is located in the outer  
572 estuary where the high salinity gradient allows more effective flocculation of the clay  
573 minerals and consequently more mud deposition on the estuary funnel floor.

574 The coarsening-upward facies pattern, observed in the subtidal parts of both tidal bars, is  
575 also very similar. It is generated by a thickening-upward trend of the sandy sedimentary  
576 structures: from ripples (facies F1a,b), to small dunes (facies F2), and to large dunes (facies  
577 F3). Nevertheless a few differences can be observed in Lower sand bar facies (F2) and the  
578 Middle sand bar facies (F3): clay drapes are more abundant in the Plassac tidal bar. Their  
579 preservation is a function of the velocity of tidal currents: in the outer estuary, on the  
580 Richard bar, stronger currents erode more clay drapes.

581 The fining-upward pattern is better observed in the Plassac tidal bar than in the Richard tidal  
582 bar (Figs 5 and 6). It is generated by a thinning-upward trend of the sandy sedimentary  
583 structures. On the inner estuary tidal bars (Plassac and also Trompeloup, see: Féniès and  
584 Tastet, 1998), the fining-upward pattern is generated by a decrease in the size of  
585 sedimentary structures, from medium-size dunes (F3), to small dunes (F5 a,b), to the ripples

586 and linsens (F6), and then to clay drapes (F7). On the outer estuary tidal bars (Richard), the  
587 Tidal flat facies (F6) and the Tidal marsh facies (F7) are not deposited; the fining-upward  
588 pattern is therefore generated only by the decrease in the dune size from medium-sized  
589 dunes (F3), to small dunes (F5a,b).

590 Quartz, feldspars and lithic grains predominate in the two bars, with sand composition  
591 ranging from litharenite to feldspathic litharenite (Fig. 2). Nevertheless, grain composition  
592 slightly differs from the two bars. The proportion of bioclastic grains is on average higher in  
593 the Richard tidal bar (6 %) compared to Plassac tidal bars (3%) with the presence of various  
594 benthic and planktonic organisms (echinoderms, foraminiferas, bivalves, Fig. 8 A-B) due to  
595 the proximity of marine sediment source. The higher salinity (18‰; Gibbs et al., 1989) in the  
596 area of the Richard tidal bar is not enough to explain a living environment for these  
597 organisms. This argues a more open marine environment for the source of these grains,  
598 probably from the tidal inlet. Clay assemblages are also slightly different: they are smectite  
599 and illite-rich for the Plassac tidal bar, and illite-rich for the Richard tidal bar (Virolle et al.,  
600 2019). Mean grain size is lower in the outer estuary (average of 153  $\mu\text{m}$  for the Richard tidal  
601 bar) than in the inner estuary tidal bar (average of 225  $\mu\text{m}$  for the Plassac tidal bar; Table 2).  
602 The Richard tidal bar is located within the muddy basin between two sand rich domains: the  
603 tidal inlet and the bay-head delta. At the beginning of the 20<sup>th</sup> century, the landward  
604 migration of the bar (Fig. 14B) associated with bioclastic component in cores tend to  
605 demonstrate an association with the tidal inlet dynamics. On the other hand, from 1950 to  
606 present day, the seaward migration suggests an affinity with the bay-head delta dynamic.  
607 Therefore, the Richard tidal bar seems to be a composite bar responding alternately to the  
608 dynamics of the tidal inlet and the bay-head delta and belonging to the muddy basin within  
609 the outer estuary funnel.

610

### 611 5.3. Distribution and evolution of clay minerals and detrital clay grain coats 612 within the tidal bars

613

#### 614 5.3.1. Clay mineral distribution in relation to hydrodynamic conditions

615

616 TEM analyses show that the clay particles forming clay coats have intermediate  
617 compositions like those obtained through weathering processes (Fig. 12D). Therefore, we  
618 postulate that these particles are detrital, and not neo-formed or authigenic. The coats are  
619 mainly composed of dioctahedral smectite and illite with lower amounts of kaolinite (Fig.  
620 12D).

621 The local increase in the water band in FTIR, as observed near the surface of the PLA-2015-C  
622 core or more deeply in the Ri-2016-W core, may be associated with an increased  
623 contribution from swelling minerals such as smectite (Figs 9 and 10). FTIR measurements  
624 using a portable spectrometer allow detecting rapidly aluminous phases such as micas or  
625 clay minerals in sands. Specific bands such as the water band at 1900 nm or the bands at  
626 2200 nm and 2253 nm, characteristic of aluminous phases, reveals local variations of clay  
627 minerals as smectite for example. Local hydrodynamic conditions along the estuary can  
628 explain this distribution (Gibbs, 1983; Chamley, 1989; McAnally and Mehta, 2000;  
629 Whitehouse, 2000; Worden and Morad, 2003). The Gironde estuary TMZ is rich in smectite  
630 and illite, which is deposited through biologically or chemically-induced flocculation  
631 (Latouche et al., 1991; Gibbs, 1983). Recent studies have shown that the decline in flood  
632 periods in the estuarine system, and the longer duration of low-river stages, maintains the  
633 TMZ in the upstream part of the estuary from the inner part of the inner estuary funnel to

634 the estuarine channels (Jalon-Rojas et al., 2015). This could explain why more smectite is  
635 deposited and preserved in the intertidal zone of the Plassac tidal bar. It may also account  
636 for the higher clay fraction content in the Plassac tidal bar than the Richard tidal bar (Table  
637 2).

638

### 639 5.3.2. Detrital clay grain coat composition, origin and distribution within modern 640 estuarine tidal bars

641

642 Detrital clay grain coat textures such as the ridged, aggregated or bridged textures observed  
643 in cores sampled along the inner and outer tidal bars (Plassac and Richard) are consistent  
644 with those reported in the intertidal zone of tidal bars of the Gironde and the Ravenglass  
645 estuaries (Virolle et al., 2019, Wooldridge et al., 2017, 2019). In the Gironde estuary, the clay  
646 mineral assemblage is relatively similar in the cores and at the surface of tidal bars (illite,  
647 smectite, chlorite and kaolinite), pointing to a relative stability in the composition of clay  
648 assemblages in the TMZ during the last centuries. The clay assemblage differs in other  
649 modern estuaries such as the Ravenglass estuary whose clay assemblage is marked by the  
650 absence of smectite and where clay mineral distribution is controlled by estuarine  
651 hydrodynamics (Wooldridge et al., 2018, Griffiths et al., 2018, 2019b). However, within both  
652 the Gironde and the Ravenglass estuaries, post-depositional processes, as early-diagenetic  
653 mineral alteration through continued weathering of silicate minerals, do not influence clay-  
654 mineral distribution patterns in near-surface sediment (Griffiths et al., 2019a and 2019b).

655 In the Gironde, coats contain other components including silt-sized quartz, carbonates and  
656 pyrite embedded within detrital clay grain coats (Figs 7 C-D and 8 C-D). Pyrite has also been  
657 observed in short cores (1 m) from the Ravenglass estuary, mainly in mud flats and mixed

658 flats in the center basin (Griffiths et al., 2018). The formation of sedimentary iron sulphides  
659 via bacterial sulphate reduction in marine systems is well known (Bernier, 1967, 1970). Even  
660 in marginal proportions (less than 1% of the total volume), it shows that iron is present in  
661 the water column of the estuary (Robert et al., 2004; Audry et al., 2007). As within the  
662 Ravensglass, carbonates abundance decrease with increasing grain size when moving toward  
663 the inner estuary (Griffiths et al., 2019b).

664 The Plassac tidal bar has, on average, more coated grain content (22% of detrital grains) than  
665 the Richard tidal bar (13%; Table 2), as is the case within surface sediments (Virolle et al.,  
666 2019).

667 Clay content and coated grain content within the Gironde estuary tidal bar deposits could be  
668 mostly related to hydrodynamic variations (as the seasonal TMZ position changes). There is  
669 no evidence of mechanical infiltration and very scarce bioturbation in the studied cores. If  
670 these post-depositional processes have occurred, they have not significantly influenced the  
671 distribution of detrital clay grain coats in surface sediment or in the vertical facies  
672 associations of the tidal bars.

673 In the intertidal zone of the Gironde estuary tidal bars and point bars, detrital clay grain  
674 coats are mostly formed through the interaction of clay minerals and exopolymeric  
675 substances (EPSs) mostly produced by diatoms (Virolle et al., 2019). EPSs may act as a glue  
676 allowing clay particles to adhere to detrital grains (Jones et al., 2017; Wooldridge et al.,  
677 2017, Virolle et al., 2019). Both optical microscopy and SEM observations confirm that  
678 diatoms are present inside clay coats in both tidal bars down to several metres below the  
679 surface (Fig. 7F, 7I and 8E). Additional studies will have to be carried out to determine  
680 whether EPSs are preserved during burial and play a part in the preservation of clay coats  
681 within tidal bars.

682

## 683       5.4.   Reservoir potential of inner and outer estuary tidal bars

684

685   The reservoir potential of the Plassac and Richard tidal bars is studied at different scales (i)  
686   macroscopic scale (dimensions and internal architecture of the bars), (ii) mesoscopic scale  
687   (facies composition), and (iii) microscopic scale (coated grain content and clay fraction).

688

689   On the macroscopic scale, the Plassac tidal bar is 4.6 km long, 1.4 km wide and the maximum  
690   sand thickness reaches 5.60 m (core PLA-2015-C, Fig. 16). The Richard tidal bar is smaller: 4  
691   km long, 300 m wide and the maximum sand thickness reaches 3.50 m (core Ri-2016-W).

692   The Gironde estuary bar size is comparable to the size of many ancient estuarine tidal bars,  
693   e.g., in the Permian Cape Hay Formation (Australia; Saïag et al., 2016), in the Early Jurassic  
694   Tilje Formation (Norway; Nordahl et al., 2006; Martinius et al., 2011) and in the Early  
695   Cretaceous Sege Formation (United States; Aschoff et al., 2016).

696   Both tidal bars are composed of stacked sand bodies, separated by muddy internal seals,  
697   which may partition the bars into different reservoir cells (Figs 5 and 6). These sand bodies  
698   may be laterally juxtaposed (Plassac tidal bar), or vertically stacked (Richard tidal bar) due to  
699   very different processes. The Plassac tidal bar is composed of two lateral accretion sand  
700   packages (facies: F2, F3 and F5a), separated by a decimetre-thick muddy layer (facies F4a),  
701   which dips gently eastward (3° dip-angle) in a direction normal to the axis of the tidal  
702   currents. Its internal architecture records the lateral migration of a single tidal bar,  
703   punctuated by phases of growth and abandonment. The Richard tidal bar is a composite  
704   geobody, made of two stacked sandy tidal bars, separated by a decimetre-thick muddy layer  
705   (Fig. 6). The lower sand body (facies F2, F3) was deposited during the lateral migration of a

706 first tidal bar. It was then abandoned, partially eroded and capped by a muddy layer (facies  
707 F4b), dipping gently eastward ( $1.5^\circ$  dip-angle). Finally, the upper sand body (facies F5b) was  
708 deposited during the lateral migration of a second tidal bar, on top of the muddy layer  
709 (facies F4b). The internal architecture of the Richard tidal bar is very similar to that of the  
710 Trompeloup tidal bar which is also composed of two stacked individual tidal bars, separated  
711 by a thick muddy layer (Féniès and Tastet, 1998).

712

713 On the mesoscopic scale, the reservoir facies of the Plassac and Richard tidal bars (facies F2,  
714 F3, F5a, F5b, Fig. 16) are mostly composed of sand dunes exhibiting variable clay drape  
715 content. Those millimetre-thick clay drapes are a few metres long and wide. In terms of  
716 reservoir capacity, those clay drapes will reduce the vertical permeabilities and could act as  
717 potential fluid and pressure baffles. The Middle bar facies (F3) could be considered as the  
718 best reservoir facies on the mesoscopic scale due to the low abundance of preserved clay  
719 drapes; the Lower sand bar facies (F2) might be the poorest quality reservoir facies due to  
720 the numerous clay drapes preserved. The Upper sand bar facies (F5) shows a noticeable  
721 difference between the inner and outer estuary tidal bars: in the Plassac tidal bar the (F5a)  
722 facies contains abundant clay drapes and mud pebbles, whereas in the Richard tidal bar, the  
723 (F5b) facies is characterized by the absence of clay drapes that would acted as baffles and  
724 therefore could be considered a better reservoir (Fig. 16).

725

726 On the microscopic scale, the distribution of detrital clay grain coats is a major parameter  
727 controlling quartz cement inhibition and the preservation of porous space if the sand bars  
728 are deeply buried (Fig. 16). On the contrary, the total volume of clays will probably result in



729 authigenic clay minerals blocking pore throats and drastically reducing permeability at great  
730 burial depths (Worden and Morad, 2003; Wooldridge et al., 2017; Griffiths et al., 2018).  
731 Those parameters are analysed in detail for each tidal bar facies (Table 2). The Middle bar  
732 facies (F3) could be considered as the best reservoir facies of both tidal bars if deeply buried,  
733 because it contains the minimum clay fraction (15 wt% and 14 wt% for Plassac and Richard  
734 respectively), while exhibiting a fairly high coated grain content (R=12%, P=23%).  
735 The Richard tidal bar has higher porosities values (*ca.* 34%) than the Plassac tidal bar (*ca.*  
736 25%). The Plassac tidal bar has a higher proportion of coated grains than the Richard tidal  
737 bar (av.: 22% vs. 13%) and the total volume of the clay fraction is higher at Plassac than at  
738 Richard (av.: 30 wt% vs. av.: 24 wt%). At Plassac, 6% of grains are coated by clay which  
739 covers 15–30% of the grain surface. At Richard, only 3% of grains are coated by clay,  
740 covering 15–30% of the grain surface (Table 2). Consequently, on the microscopic scale, the  
741 Richard tidal bar will provide the best reservoir potential if deeply buried, with about 15% of  
742 coated grain and about 25% of total volume of clays. Besides, porosity can be enhanced  
743 through carbonates dissolution as it can occur in Richard tidal bar, richer in carbonates.  
744 Remaining porosity during subsequent compaction may be preserved through early  
745 carbonate cement formation that can increase the mechanical strength of sediments  
746 (Morris et al., 2006). Therefore, as it can be observed in the Ravenglass estuary, better  
747 reservoir quality may be found in estuarine depositional environments that initially  
748 contained a small amount of carbonate material (Griffiths et al., 2019). Outer estuarine  
749 tidal bars might therefore be the best prospects for reservoir qualities at great depth. The  
750 Plassac tidal bar may experience more intense matrix formation during eodiagenesis owing  
751 to plastic deformation and compaction of ductile grains (clay drapes and mud pebbles)

752 between rigid grains (Morad et al., 2010). Higher coated grain content can also obstruct  
753 porosity throats during compaction affecting reservoir qualities.

## 754 6. Conclusion

755 This multi-scale study aims to better understand processes governing the facies associations,  
756 reservoir architecture, and distribution of detrital clay grain coats and clay minerals within  
757 two tidal bars deposited in the Gironde estuary: the Plassac tidal bar in the inner estuary  
758 funnel and the Richard tidal bar in the outer estuary funnel. Although these tidal bars are 40  
759 km apart, they are characterized by similar vertical facies associations which result from  
760 specific hydrodynamic processes that are generated in very turbid estuaries.

761 On a larger scale, the overall dimensions of both tidal bars are comparable to those  
762 observed in ancient estuaries. They are 4 to 5 km long, 300 to 1400 m wide and their  
763 maximum individual sand thickness ranges from 3.5 to 5.6 m.

764 Their internal architecture shows that the two tidal bars are composite geobodies made of  
765 stacked sand units, separated by muddy internal seals partitioning the bars into different  
766 reservoir cells. For both bars, the alternating periods of sand deposition (Lateral Accretion  
767 Sand Packages or individual tidal bars) and mud deposition (muddy internal seals) may be  
768 controlled by short term (multi-annual) climatic cycles.

769 On a smaller scale, detrital clay grain coats are observed from the top to the base of both  
770 tidal bars, in the entire intertidal and subtidal zones. Coats are mainly composed of clay  
771 minerals (dioctahedral smectite, illite, kaolinite and chlorite), associated with a minor  
772 proportion of other elements such as silt-sized quartz, coccoliths, pyrite or diatoms frustules.  
773 Clay minerals can be rapidly detected using a portable spectrometer. Globally, clay  
774 assemblage is the same from the top to the bottom of tidal bars. Variations of specific bands

775 as the ones at 1900 nm, 2200 nm or 2253 nm reveal local variations of some clay minerals as  
776 smectite. The clay fraction and coated grain content are higher in the inner estuary Plassac  
777 tidal bar than in the outer estuary Richard tidal bar probably due to the more regular  
778 presence of TMZ in the Plassac area. Tidal bars deposited in the outer estuary present the  
779 optimum coated grain content (about 15% of grains are coated), coat coverage (extent of  
780 grain covered by clays reach about 5–15%) and clay fraction volume (about 25%). Outer  
781 estuary tidal bars are more likely to offer the best reservoir quality in terms of porosity and  
782 permeability after burial. This study has shown that multi-scale processes can influence  
783 reservoirs quality distribution and prediction at great depth. Results may be used to better  
784 predict and understand sandstone reservoir quality in similar estuarine sandstones  
785 reservoirs.

786

## 787 **ACKNOWLEDGMENTS**

788 This work is the result of collaborative project No P04980 CLAYCOAT “CLAY COATING in  
789 shallow marine clastic deposits to improve reservoir quality prediction” between University  
790 Paris-Sud, Bordeaux INP, University of Bordeaux Montaigne, University of Poitiers and ENGIE  
791 (Neptune Energy since 2018). This study has benefitted greatly from ENGIE and Neptune  
792 Energy funding. The authors would also like to thank the Bordeaux Harbour Authorities for  
793 providing bathymetric data of the Gironde estuary. We thank Julius Nouet (GEOPS) for  
794 assistance with SEM observations. We are grateful to Léa Pigot (ENSEGID), Valérie Godard  
795 (GEOPS) and Philippe Blanc (Lithologie Bourgogne) for high-quality thin sections. We also  
796 wish to thank the “Sediment Archive Analysis” Platform at the EPOC laboratory (Bordeaux,  
797 France), and especially Isabelle Billy, Pascal Lebleu and Olivier Ther for their support during  
798 the core description. We thank Marc Massault for assistance during graphite preparation

799 and during  $^{14}\text{C}$  counting performed at Gif-sur-Yvette using AMS ECHOMICADAS. And finally,  
800 we thank N'Guessan Essey and Aude Cumont from the University of Poitiers, Flora  
801 Guillemaut and Violaine Gascuel from the ENSEGID (Bordeaux INP) for their contributions to  
802 this study. We also thank the associate editor, Andrew Green, Bernadette Tessier and an  
803 anonymous reviewer who provided insightful and helpful comments that improved the final  
804 manuscript.

805

## 806 **References**

807 Aase, N.E., Bjorkum, P.A., Nadeau, P.H., 1996. The Effect of Grain-Coating Microquartz on  
808 Preservation of Reservoir Porosity. AAPG Bulletin 80 (10), 1654–1673.

809 Allen, G.P., 1972. Etude des processus sédimentaires dans l'estuaire de la Gironde. Thèse  
810 Doctorat des Sciences, Université de Bordeaux I, No. 353, 314 pp.

811 Allen, G.P., Bonnefille, R., Courtois, G., Migniot, C., 1974. Processus de sédimentation des  
812 vases dans l'estuaire de la Gironde Contribution d'un traceur radioactif pour l'étude du  
813 déplacement des vases. La Houille Blanche 1-2, 129-136.

814 Allen, G.P., Sauzay, G., Castaing, P., Jouanneau, J.M., 1977. Transport and deposition of  
815 suspended sediment in the Gironde Estuary, France. Estuarine Processes 2, 63-81.

816 Allen, G.P., 1991. Sedimentary processes and facies in the Gironde estuary: a recent model  
817 for macrotidal estuarine systems. In: Clastic Tidal Sedimentology (Eds R.A. Rahmani, D.G.  
818 Smith, G.E. Reinson and B.A. Zaitlan), Memoir 16, 29-39.

819 Allen, G.P., Posamentier, H.W., 1994. Transgressive facies and sequence architecture in  
820 mixed tide-and wave-dominated incised valleys: example from the Gironde Estuary, France.  
821 In: Incised-valley Systems: Origins and Sedimentary Sequences (Eds R.W. Dalrymple, R. Boyd  
822 and B.A. Zaitlin), SEPM Special Publication 51, 225-240.

- 823 Allen, G.P., Salomon, J.C., Bassoullet, P., Du Penhoat, Y., De Grandpre, C., 1980. Effects of  
824 tides on mixing and suspended sediment transport in macrotidal estuaries. *Sedimentary*  
825 *Geology* 26, 69–90.
- 826 Aschoff, J.L., Olariu, C., Steel, R.J., 2018. Recognition and significance of bayhead delta  
827 deposits in the rock record: A comparison of modern and ancient systems. *Sedimentology*  
828 65, 62–95.
- 829 Audry, S., Blanc, G., Schäfer, J., Robert, S., 2007. Effect of estuarine sediment resuspension  
830 on early diagenesis, sulfide oxidation and dissolved molybdenum and uranium distribution in  
831 the Gironde estuary, France. *Chemical Geology* 238, 149-167.
- 832 Berner, R., 1967. Thermodynamic stability of sedimentary iron sulfides. *American Journal of*  
833 *Science* 265, 773-785.
- 834 Berner, R., 1970. Sedimentary pyrite formation. *American Journal of Science* 268, 1–23.
- 835 Beaufort, D., Rigault, C., Billon, S., Billault, V., Inoue, A., Inoue, S., Patrier, P., 2015. Chlorite  
836 and chloritization processes through mixed-layer mineral series in low-temperature  
837 geological systems-a review. *Clay Minerals* 50, 497-523.
- 838 Billy, J., Chaumillon, E., Féliès, H., Poirier, C., 2012 Tidal and fluvial controls on the  
839 morphological evolution of a lobate estuarine tidal bar: The Plassac Tidal Bar in the Gironde  
840 Estuary (France). *Geomorphology* 169–170, 86–97.
- 841 Bjørlykke, K., 2014. Relationships between depositional environments, burial history and  
842 rock properties. Some principal aspects of diagenetic process in sedimentary basins.  
843 *Sedimentary Geology* 301, 1–14.
- 844 Bjorlykke, K., Egeberg, P.K., 1993. Quartz cementation in sedimentary basins. *AAPG Bulletin*  
845 77, 1538–1548.
- 846 Bloch, S., Lander, R.H., Bonnell, L., 2002. Anomalously high porosity and permeability in

- 847 deeply buried sandstone reservoirs: Origin and predictability. AAPG Bulletin 86, 303-328.
- 848 Bonneton, P., Bonneton, N., Parisot, J.-P., Castelle, B., 2015. Tidal bore dynamics in funnel-  
849 shaped estuaries. Journal of Geophysical Research: Oceans 120, 923–941.
- 850 Castaing, P., 1981. Le transfert à l'océan des suspensions estuariennes : cas de la Gironde.  
851 Mémoires de l'Institut De Géologie Du Bassin D'Aquitaine 12, 530 p.
- 852 Chamley, H., 1989. Clay Sedimentology. Springer Berlin Heidelberg, Berlin, Heidelberg.
- 853 Chanson, H., Reungoat, D., Simon, B., Lubin, P., 2011. High-frequency turbulence and  
854 suspended sediment concentration measurements in the Garonne River tidal bore. Estuarine  
855 and Coastal Shelf Science 95, 298-306.
- 856 Chaumillon, E., Féliès, H., Billy, J., Breilh, J.-F., Richetti, H., 2013. Tidal and fluvial controls on  
857 the internal architecture and sedimentary facies of a lobate estuarine tidal bar (The Plassac  
858 Tidal Bar in the Gironde Estuary, France). Marine Geology 346, 58–72.
- 859 Dalrymple, R.W., Zaitlin, B.A., Boyd, R., 1991. Estuarine facies models: Conceptual basis and  
860 stratigraphic implications. Journal of Sedimentary Research 62, 1130–1146.
- 861 Deschamps, R., Guy, N., Preux, C., Lerat, O., 2012. Analysis of Heavy Oil Recovery by Thermal  
862 EOR in a Meander Belt: From Geological to Reservoir Modeling. Oil Gas Sci. Technol. – Revue  
863 D'IFP Energies Nouvelles 67, 999–1018.
- 864 Doxaran, D., Froidefond, J.-M., Castaing, P., Babin, M., 2009. Dynamics of the turbidity  
865 maximum zone in a macrotidal estuary (the Gironde, France): Observations from field and  
866 MODIS satellite data. Estuarine, Coastal and Shelf Science 81, 321–332.
- 867 Ehrenberg, S.N., 1989. Assessing the Relative Importance of Compaction Processes and  
868 Cementation to Reduction of Porosity in Sandstones: Discussion; Compaction and Porosity  
869 Evolution of Pliocene Sandstones, Ventura Basin, California: Discussion. AAPG Bulletin 73,  
870 1274-1276.

- 871 Ehrenberg, S.N., 1993. Preservation of anomalously high porosity in deeply buried  
872 sandstones by grain coating chlorite: examples from the Norwegian continental shelf. AAPG  
873 Bulletin 77, 1260–1286.
- 874 Etcheber, H., Jouanneau, J.M., Latouche, C., Azoef, P., Caillot, A., Hoslin, R., 1980.  
875 L'expérience "double marquage de vase en Gironde". Contribution à la connaissance du  
876 devenir d'une pollution métallique en estuaire. *Oceanologica acta* 3, 477-486.
- 877 Etcheber, H., Schmidt, S., Sottolichio, A., Maneux, A., Chabaux, G., Escalier, J.M, Wennekes,  
878 H., Derrienic, H., Schmeltz, M., Quéméner, L., Repecaud, M., Woerther, P., Castaing, P.,  
879 2011. Monitoring water quality in estuarine environments: lessons from the MAGEST  
880 monitoring program in the Gironde fluvial-estuarine system. *Hydrology and Earth System  
881 Sciences* 15, 831-840.
- 882 Féliès, H., Resseguier, A.D., Tastet, J.-P., 1999. Intertidal clay-drape couplets (Gironde  
883 estuary, France). *Sedimentology* 46, 1–15.
- 884 Féliès, H., Tastet, J.-P., 1998. Facies and architecture of an estuarine tidal bar (the  
885 Trompeloup bar, Gironde Estuary, SW France). *Marine Geology* 150, 149–169.
- 886 Féliès, H., Lericolais, G., Posamentier, H.W., 2010. Comparison of wave- and tide-dominated  
887 incised valleys: specific processes controlling systems tract architecture and reservoir  
888 geometry. *Bulletin of the French Geological Society* 181, 171-181
- 889 Gascuel, V., 2017. Analyse de l'évolution morphologique de barres de marées de l'estuaire  
890 de la Gironde : Etude del'évolution des barres de Bordeaux, Plassac, Trompeloup, et Richard  
891 en relation avec les processus sédimentaires et anthropiques. Mem. Stage 2eme année en  
892 école d'ingénieur, ENSEGID, Bordeaux INP.
- 893 Gibbs, R.J., 1983. Coagulation rates of clay minerals and natural sediments. *Journal of  
894 Sedimentary Research* 53, 1193-1203.

- 895 Gibbs, R.J., Tshudy, D.M., Konwar, L. and Martin, J., 1989. Coagulation and transport of  
896 sediments in the Gironde Estuary. *Sedimentology* 36, 987–999.
- 897 Gascuel, V., 2017. Analyse de l'évolution morphologique de barres de marées de l'estuaire  
898 de la Gironde : Etude de l'évolution des barres de Bordeaux, Plassac, Trompeloup, et Richard  
899 en relation avec les processus sédimentaires et anthropiques. Mem. Stage 2<sup>ème</sup> année en  
900 école d'ingénieur, ENSEGID, Bordeaux INP, 85 p.
- 901 Gibert, E., Bergonzini, L., Massault, M., Williamson, D., 2002. AMS-14C chronology of 40.0 cal  
902 ka BP continuous deposits from a crater lake (Lake Massoko, Tanzania) Modern water  
903 balance and environmental implications. *Paleogeography Paleoclimatology Paleoecology*  
904 187, 307–322.
- 905 Gould, K., Pe-Piper, G., Piper, J.W., 2010. Relationship of diagenetic chlorite rims to  
906 depositional facies in Lower Cretaceous reservoir sandstones of the Scotian Basin,  
907 *Sedimentology* 57, 587-610.
- 908 Griffiths, J., Worden, R. H., Wooldridge, L. J., Utley, J. E., Duller, R. A., 2018. Detrital clay  
909 coats, clay minerals, and pyrite: a modern shallow-core analogue for ancient and deeply  
910 buried estuarine sandstones. *Journal of Sedimentary Research*, 881, 1205-1237.
- 911 Griffiths, J., Worden, R. H., Wooldridge, L. J., Utley, J. E., Duller, R. A., Edge, R. L., 2019a.  
912 Estuarine clay mineral distribution: Modern analogue for ancient sandstone reservoir quality  
913 prediction. *Sedimentology* 66, 2011-2047.
- 914 Griffiths, J., Worden, R. H., Wooldridge, L. J., Utley, J. E., Duller, R. A., 2019b. Compositional  
915 variation in modern estuarine sands: predicting major controls on sandstone reservoir  
916 quality. *AAPG Bulletin* 103, 797-833.
- 917 Grim, R.E., 1942. Modern concepts of clay materials. *The Journal of Geology* 50, 225–275.
- 918 Guillemaut, F., 2016. Etude faciologique et pétrographique des barres de marée (Plassac,



- 919 Gironde) : Prédiction de la distribution du coating argileux. Mem. Stage 3<sup>eme</sup> année en école  
920 d'ingénieur, ENSEGID, Bordeaux INP, 59 p.
- 921 Jackson, M.D., Muggeridge, A.H., Yoshida, S., Johnson, H.D., 2003. Upscaling Permeability  
922 Measurements Within Complex Heterolithic Tidal Sandstones. *Mathematical Geology* 35,  
923 499-520.
- 924 Jackson, M.D., Yoshida, S., Muggeridge, A.H., Johnson, H.D., 2005. Three-dimensional  
925 reservoir characterization and flow simulation of heterolithic tidal sandstones. *AAPG Bulletin*  
926 89, 507–528.
- 927 Jalón-Rojas, I., Schmidt, S., Sottolichio, A., 2015. Turbidity in the fluvial Gironde Estuary  
928 (southwest France) based on 10-year continuous monitoring: sensitivity to hydrological  
929 conditions. *Hydrology and Earth System Sciences* 19, 2805–2819.
- 930 Jones, S., 2017. Goo, glue, and grain binding: importance of biofilms for diagenesis in  
931 sandstones. *Geology* 45, 959-960.
- 932 Latouche, C., Jouanneau, J.M., Lapaquellerie, Y., Maillet, N., Weber, O., 1991. Répartition des  
933 minéraux argileux sur le plateau continental Sud-Gascogne. *Oceanologica Acta. Actes du*  
934 *Colloque International sur l'environnement des mers épicontinentales*, Lille, 155-161.
- 935 Legler, B., Johnson, H.D., Hampson, G.J., Massart, B.Y.G., Jackson, C.A.-L., Jackson, M.D., El-  
936 Barkooky, A., Ravnas, R., 2013. Facies model of a fine-grained, tide-dominated delta: Lower  
937 Dir Abu Lifa Member (Eocene), Western Desert, Egypt. *Sedimentology* 60, 1313–1356.
- 938 Lericolais, G., Féliès, H., Tastet, J.-P., Berné, S., 1998. Reconnaissance par stratigraphie  
939 sismique haute résolution de la paléovallée de la Gironde sur le plateau continental.  
940 *Comptes Rendus Académie Sci.-Ser. IIA-Earth and Planetary Science* 326, 701–708.
- 941 Mallet, C., Howa, H.L., Garlan, T., Sottolichio, A., Le Hir, P., 2000. Residual Transport Model in  
942 Correlation with Sedimentary Dynamics over an Elongate Tidal Sandbar in the Gironde

- 943 Estuary (Southwestern France). *Journal of Sedimentary Research* 70, 1005–1016.
- 944 Martinius, A.W., Ringrose, P.S., Brostrom, C., Elfenbein, C., Naess, A., Ringas, J.E., 2005.
- 945 Reservoir challenges of heterolithic tidal sandstone reservoirs in the Halten Terrace, mid-
- 946 Norway. *Petroleum Geoscience* 11, 3–16.
- 947 Martinius, A.W., Berg, J.H., Buller, A.T., 2011. Atlas of sedimentary structures in estuarine
- 948 and tidally-influenced river deposits of the Rhine-Meuse-Scheldt system: their application to
- 949 the interpretation of analogous outcrop and subsurface depositional systems. EAGE
- 950 Publications, Houten, 298 p.
- 951 Massart, B.Y.G., 2014. Improved characterisation and modelling of heterolithic tidal
- 952 sandstone reservoirs. Imperial college London, London, 224 p.
- 953 McAnally, W.H., Mehta, A.J., 2000. Aggregation rate of fine sediment. *Journal of Hydraulic*
- 954 *Engineering* 126, 883–892.
- 955 Meunier, A., Velde, B., 1989. Solid solutions in I/S mixed-layer minerals and illite. *American*
- 956 *Mineralogist* 74, 1106-1112.
- 957 Morad, S., Al-Ramadan, K., Ketzer, J.M., De Ros, L.F., 2010. The impact of diagenesis on the
- 958 heterogeneity of sandstone reservoirs: a review of the role of depositional facies and
- 959 sequence stratigraphy. *AAPG Bulletin* 94, 1267-1309.
- 960 Morris, J. E., Hampson, G. J., Johnson, H. D., 2006. A sequence stratigraphic model for an
- 961 intensely bioturbated shallow-marine sandstone: the Bridport Sand Formation, Wessex
- 962 Basin, UK: *Sedimentology* 53, 1229-1263.
- 963 Musial, G., Reynaud, J.-Y., Gingras, M.K., Féliès, H., Labourdette, R., Parize, O., 2012.
- 964 Subsurface and outcrop characterization of large tidally influenced point bars of the
- 965 Cretaceous McMurray Formation (Alberta, Canada). *Sedimentary Geology* 279, 156–172.

- 966 Nordahl, K., Ringrose, P.S., Wen, R., 2005. Effective permeability of a heterolithic tidal  
967 reservoir interval using a process-orientated modelling tool. *Petroleum Geoscience* 11, 17–  
968 28.
- 969 Nordahl, K., Martinius, A.W., Kritski, A., 2006. Time-series analysis of a heterolithic, ripple-  
970 laminated deposit (Early Jurassic, Tilje Formation) and implications for reservoir modelling.  
971 *Marine Geology* 235, 255–271.
- 972 Nordahl, K., Ringrose, P.S., 2008. Identifying the Representative Elementary Volume for  
973 Permeability in Heterolithic Deposits Using Numerical Rock Models. *Mathematical*  
974 *Geoscience* 40, 753–771.
- 975 Olariu, M.I., Olariu, C., Steel, R.J., Dalrymple, R.W, Martinius, A.W., 2012. Anatomy of a  
976 laterally migrating tidal bar in front of a delta system: Esdolomada Member, Roda  
977 Formation, Tremp-Graus Basin, Spain: Esdolomada tidal bar. *Sedimentology* 59, 356–378.
- 978 Pe-Piper, G., Weir-Murphy, S., 2008. Early diagenesis of inner shelf phosphorite and iron-  
979 silicate minerals, Lower Cretaceous of Orpheus graben, southeastern Canada: implications  
980 for the origin of chlorite rims. *AAPG Bulletin* 92, 1153–1168.
- 981 Pittman, E.D., Larese, R.E., Heald, M.T., 1992. Origin, Diagenesis, and Petrophysics of Clay  
982 Minerals in Sandstones. (Eds Houseknecht, D.W., Pittman, E.D). *SEPM Special Publication* 47,  
983 241-255.
- 984 Reineck, H.-E., Wunderlich, F., 1968. Classification and origin of flaser and lenticular bedding.  
985 *Sedimentology* 11, 99–104.
- 986 Ringrose, P., Nordahl, K., Wen, R., 2005. Vertical permeability estimation in heterolithic tidal  
987 deltaic sandstones. *Petroleum Geoscience* 11, 29–36.

- 988 Robert, S., Blanc, G., Schäfer, J., Lavaux, G., Abril, G., 2004. Metal mobilization in the Gironde  
989 Estuary (France): the role of the soft mud layer in the maximum turbidity zone. *Marine*  
990 *Chemistry* 87, 1-13.
- 991 Roduit, N., 2007. JMicroVision: un logiciel d'analyse d'images pétrographiques polyvalent.  
992 Section des Sciences de la Terre, Université de Genève, Genève, 129 p.
- 993 Saiag, J., Brigaud, B., Portier, É., Desaubliaux, G., Bucherie, A., Miska, S., Pagel, M., 2016.  
994 Sedimentological control on the diagenesis and reservoir quality of tidal sandstones of the  
995 Upper Cape Hay Formation (Permian, Bonaparte Basin, Australia). *Marine and Petroleum*  
996 *Geology* 77, 597–624.
- 997 Savoye, N., David, V., Morisseau, F., Etcheber, H., Abril, G., Billy, I., Charlier, K., Oggian, G.,  
998 Derriennic, H., Sautour, B., 2012. Origin and composition of particulate organic matter in a  
999 macrotidal turbid estuary: The Gironde Estuary, France. *Estuarine, Coastal and Shelf Science*  
1000 108, 16–28.
- 1001 Shchepetkina, A., Gingras, M.K., Pemberton, S.G., 2016. Sedimentology and ichnology of the  
1002 fluvial reach to inner estuary of the Ogeechee River estuary, Georgia, USA. *Sedimentary*  
1003 *Geology* 342, 202–217.
- 1004 Shchepetkina, A., Gingras, M. K., Pemberton, S. G., 2018. Modern observations of floccule  
1005 ripples: petitcodiac River estuary, New Brunswick, Canada. *Sedimentology* 65 , 582-596.
- 1006 Sottolichio, A., Castaing, P., 1999. A Synthesis on seasonal dynamics of highly-concentrated  
1007 structures in the Gironde estuary. *Compte Rendu de l'Académie des Sciences- Séries IIA-*  
1008 *Earth and Planetary Science* 329, 795–800.
- 1009 Sottolichio, A., Castaing, P., Etcheber, H., Maneux, E., Schmeltz, M., Schmidt, S., 2011.  
1010 Observations of suspended sediment dynamics in a highly turbid macrotidal estuary, derived  
1011 from continuous monitoring. *Journal of Coastal Research* 64, 1579-1583.

- 1012 Storvoll, V., Bjørlykke, K., Karlsen, D., Saigal, G., 2002. Porosity preservation in reservoir  
1013 sandstones due to grain-coating illite: a study of the Jurassic Garn Formation from the Kristin  
1014 and Lavrans fields, offshore Mid-Norway. *Marine and Petroleum Geology* 19, 767–781.
- 1015 Stricker, S., Jones, S.J., 2018. Enhanced porosity preservation by pore fluid overpressure and  
1016 chlorite grain coatings in the Triassic Skagerrak, Central Graben, North Sea, UK. *Geological*  
1017 *Society London Special Publication* 435, 321–341.
- 1018 Taylor, T.R., Kittridge, M.G., Winefield, P., Bryndzia, L.T., Bonnell, L.M., 2015. Reservoir  
1019 quality and rock properties modeling – Triassic and Jurassic sandstones, greater Shearwater  
1020 area, UK Central North Sea. *Marine and Petroleum Geology* 65, 1–21.
- 1021 Tessier, B., Billeaud, I., Sorrel, P., Delsinne, N., Lesueur, P., 2012. Infilling stratigraphy of  
1022 macrotidal tide-dominated estuaries. Controlling mechanisms: Sea-level fluctuations,  
1023 bedrock morphology, sediment supply and climate changes (The examples of the Seine  
1024 estuary and the Mont-Saint-Michel Bay, English Channel, NW France). *Sedimentary*  
1025 *Geology* 279, 62-73.
- 1026 Virolle, M., Brigaud, B., Bourillot, R., Féliès, H., Portier, E., Duteil, T., Nouet, J., Patrier, P.,  
1027 Beaufort, D., 2019. Detrital clay grain coats in estuarine clastic deposits: origin and spatial  
1028 distribution within a modern sedimentary system, the Gironde Estuary (south-west France).  
1029 *Sedimentology* 66, 859-894.
- 1030 Visser, M. J., 1980. Neap-spring cycles reflected in Holocene subtidal large-scale bedform  
1031 deposits: a preliminary note. *Geology* 8, 543-546.
- 1032 Weber, K. J., 1986. How heterogeneity affects oil recovery. In: *Reservoir Characterization*.  
1033 Eds Lake, L.W. and Carroll, H.B. Academic Press, New York, NY, 487-544.
- 1034 Whitehouse, R., Soulsby, R., Roberts, W., Mitchener, H., 2000. Dynamics of estuarine muds:  
1035 a manual for practical applications. Telford, London, 232 p.

- 1036 Wood, L.J., 2004. Predicting Tidal Sand Reservoir Architecture Using Data from Modern and  
1037 Ancient Depositional Systems. AAPG Memoir 80, 45–66.
- 1038 Wooldridge, L.J., Worden, R.H., Griffiths, J., Utley, J.E.P., 2017a. Clay-Coated Sand Grains In  
1039 Petroleum Reservoirs: Understanding Their Distribution Via A Modern Analogue. Journal of  
1040 Sedimentary Research 87, 338–352.
- 1041 Wooldridge, L. J., Worden, R. H., Griffiths, J., Thompson, A., Chung, P., 2017b. Biofilm origin  
1042 of clay-coated sand grains. Geology 45, 875-878.
- 1043 Wooldridge, L. J., Worden, R. H., Griffiths, J., Utley, J. E., 2019. How To Quantify Clay-Coat  
1044 Grain Coverage in Modern and Ancient Sediments. Journal of Sedimentary Research 89, 135-  
1045 146.
- 1046 Worden, R.H., Morad, S., 2003. Clay minerals in sandstones: controls on formation,  
1047 distribution and evolution, in: Worden, R.H., Morad, S. (Eds.), Clay mineral cements in  
1048 sandstones. Special Publication of the International Association of Sedimentologists.  
1049 Blackwells, Oxford, pp. 3-41.
- 1050 Yoshida, S., Johnson, H.D., Gupta, R., Martinius, A.W. (Eds.), 1999. Advanced Reservoir  
1051 Characterization for the 21st Century: 19th Annual. Presented at the GCSSEPM Foundation  
1052 19th Annual Research Conference Advanced Reservoir Characterization, Society of Economic  
1053 Paleontologists and Mineralogists, 100–108.

1054  
1055

1056 **FIGURE CAPTIONS**

1057 **Figure 1:** Study area location with simplified sedimentological map of the Gironde estuary  
1058 (France). Zooms of the two tidal bars are illustrated: the elongated Richard tidal bar on the  
1059 left and the lobate tidal bar on the right with sedimentary environments replaced on

1060 pictures. Bathymetric maps originate from the Atlantic Port of Bordeaux bathymetric map  
1061 that cover the entire estuary. *2 columns fitting image*

1062

1063 **Figure 2:** Petrographic composition of the framework sand grains from both tidal bars  
1064 plotted on a QFL (Q- Quartz, F- Feldspars, L- Lithic fragment) diagram (after Folk, 1980). *1.5*  
1065 *column fitting image*

1066

1067 **Figure 3:** Synthetic log representative of the Plassac tidal bar vertical facies successions. The  
1068 log is coloured according to the alternating sandy or clayey facies. Pictures in the middle  
1069 illustrate the surface equivalent and position of facies described in cores. Illustrations on the  
1070 right show representative sections of described facies with their interpretation in terms of  
1071 sedimentary structures. LWST = Low Water of Spring Tides. *2 columns fitting image*

1072

1073 **Figure 4:** Synthetic log representative of the Richard tidal bar vertical facies successions. The  
1074 log is coloured according to the facies. Pictures in the middle illustrate the surface  
1075 equivalent and position of facies described in cores. Illustrations on the right show  
1076 representative sections of described facies with their interpretations in terms of  
1077 sedimentary structures. LWST = Low Water of Spring Tides. *2 columns fitting image*

1078

1079 **Figure 5:** Plassac tidal bar cross-section showing correlation between cores and the internal  
1080 architecture of the tidal bar. Carbon 14 datings are also placed alongside cores. Correlations  
1081 lines are timelines, because they are coherent with the very high resolution seismic lines  
1082 shot across the bar (see Chaumillon at al., 2013, Fig. 3A, line GiRaFS\_65). Ages are not

1083 considered to be a good correlation tool as the organic matter debris may have been  
1084 initially deposited much before the genesis of the bar in an upstream location (e.g. estuarine  
1085 channels) and then eroded, transported downstream and incorporated into the tidal bar.

1086 LWST = Low Water of Spring Tides. *2 columns fitting image*

1087  
1088 **Figure 6:** Richard tidal bar cross-section showing correlation between cores and the internal  
1089 architecture of the tidal bar. Carbon 14 datings are also placed alongside cores. Correlations  
1090 are mainly based on facies observations. LWST = Low Water of Spring Tides. *2 columns*  
1091 *fitting image*

1092

1093 **Figure 7:** Representative microphotographs under optical microscope and SEM showing  
1094 grain composition and the textural characteristics of sand coats within the Plassac tidal bar.  
1095 A-B) Microphotographs showing quartz (Qz), Feldspars (Fd) and lithic (Li) detrital grains and  
1096 brown detrital clay minerals surrounding framework grains, forming Detrital Clay Grain Coats  
1097 (DCGC) with partial clay drapes, aggregates or bridges between grains (arrows; from facies  
1098 F3). C) Coat (outline in red) with pyrite embedded within clay minerals (from facies F3). D)  
1099 Same picture taken with reflected light device highlighting the framboidal pyrite embedded  
1100 within the detrital clay grain coat. E) SEM picture showing aggregates at the surface of a  
1101 quartz grain forming detrital clay grain coats (from facies F5a). F) Zoom of picture E on an  
1102 aggregate showing a diatom embedded within clay minerals. G) Bridge texture composed of  
1103 clay minerals associated with other components such as silt-sized quartz grains (from facies  
1104 F5a). H) Zoom from box number 1 in the bridge showing a mix of clay minerals and silts. I)  
1105 Zoom from box number 2 showing a diatom on the quartz grain surface. *2 columns fitting*  
1106 *image*



1107

1108 **Figure 8:** Representative microphotographs under optical microscope and SEM showing

1109 grain composition and the textural characteristics of sand coats within the Richard tidal bar.

1110 A-B) Microphotographs showing quartz (Qz), Feldspars (Fd), lithic (Li) detrital grains including

1111 carbonated elements of holoturian spicules and probably echinoderms (Ec) and brown

1112 detrital clay minerals surrounding framework grains, showing aggregates or forming bridges

1113 between grains (arrows; from facies F3). C) Detrital clay grain coat with pyrites embedded

1114 within clay minerals (from facies F5b). D) Same picture taken with reflected light device

1115 highlighting the framboidal pyrites embedded within the detrital clay grain coat. E)

1116 Microphotograph showing on a same picture detrital clay grain coats formed by aggregates

1117 or partial clay drapes surrounding the grain including a diatom in the grain surface (from

1118 facies F5b). F) SEM pictures showing aggregated detrital clay grain coats at the surface of

1119 quartz grains covering a more or less large surface area (from facies F3). G) SEM pictures

1120 showing aggregated detrital clay grain coats at the surface of a quartz grain (from facies

1121 F5b). H-I) Zoom from box number 1 and 2 showing carbonated elements as coccoliths or

1122 diatoms skeleton embedded within clay minerals. *2 columns fitting image*

1123

1124 **Figure 9:** Evolution of mean grain size, surface area of clay minerals from XRD semi-

1125 quantifications, coated grain content and FTIR measurements along the three cores of the

1126 Plassac tidal bar. Sand rich facies are in yellow while muddy facies are in grey. The surfaces

1127 area from the diffractograms were reduced to the percentage of fine fraction measured in

1128 the sample. LWST = Low Water of Spring Tides. *2 columns fitting image*

1129

1130 **Figure 10:** Evolution of mean grain size, surface area of clay minerals from XRD semi-  
1131 quantifications, coated grain content and FTIR measurements along the three cores of the  
1132 Richard tidal bar. Sand rich facies are in yellow while muddy facies are in grey. The surfaces  
1133 area from the diffractograms were reduced to the percentage of fine fraction measured in  
1134 the sample. LWST = Low Water of Spring Tides. *2 columns fitting image*

1135

1136 **Figure 11:** Average coated grain content per facies with coat coverage classes associated.  
1137 The sum of the coat coverage classes gives the total coated grain content for each facies  
1138 indicated above the histograms. *2 columns fitting image*

1139

1140 **Figure 12:** A) X-Ray diffractogram showing clay minerals identifiable within the Plassac tidal  
1141 bar with no treatment (red line) or after ethylene-glycol saturation (blue line). B) X-Ray  
1142 diffractogram showing clay minerals identifiable within the Richard tidal bar with no  
1143 treatment (purple line) or after ethylene-glycol saturation (green line). C) Infra-red (SWIR)  
1144 spectra on some Plassac tidal bars samples. D) Results from TEM analysis and plotted in the  
1145  $M+4Si-R2+$ . *2 columns fitting image*

1146

1147 **Figure 13:** Plate illustrating some hydrodynamic parameters in the Gironde estuary that may  
1148 influence facies deposition. A) Measurements at PK 55 in the area of the Trompeloup tidal  
1149 bar near the estuary funnel bottom showing the Fluid Mud Zone (FMZ). Erosion  
1150 preferentially occurs at mid-ebb and mid-flood, at high current velocities, whereas tidal  
1151 slacks are periods of deposition. B) Seasonal movement of the FMZ along the estuary  
1152 influenced by river discharge variations (modified from Allen et al., 1974). C) Tidal current

1153 velocity model along a cross-section normal to the Plassac tidal bar and showing tidal  
1154 current evolution with depth and along the two spits of the bar. *2 columns fitting image*

1155

1156 **Figure 14:** A) Bathymetric digital elevation models of the Plassac tidal bar from 1963 to 1983,  
1157 showing the seaward migration of sand bodies (mini flood lobes) and their merging with the  
1158 eastern spit of the bar (modified from Chaumillon et al., 2013). B) Bathymetric evolution  
1159 model of the Richard tidal bar computed after bathymetric maps analysis, showing the  
1160 landward and westward migration from 1901 to 1968 followed by a seaward and eastward  
1161 migration and extension of the bar from 1968 to 1996. The present-day location is based on  
1162 arian pictures from Google Earth. *2 columns fitting image*

1163

1164 **Figure 15:** Mean river discharges per year from 1925 to 1996 in the Gironde estuary. Green  
1165 bars indicate an overall period of low-river discharges *2 columns fitting image*

1166

1167 **Figure 16:** Large scale to small scale reservoir models of the two tidal bars. Location in the  
1168 estuary, diagram from an aerial point of view of the bars, cross-section within the bars  
1169 showing schematically the internal architecture of the reservoir units, vertical association of  
1170 synthetic facies with representative core sections and microscopic pictures of the best  
1171 reservoir facies with coatings associated with detrital grains. The best reservoir geobody is  
1172 located in the outer estuary in the Richard tidal bar with two superimposed sand units  
1173 separated by a single clay layer discontinuity. Abbreviations mean: Qz: Quartz, Li: Lithic  
1174 grains, Fd: Feldspar, Mu: Muscovite, Bc: Bioclast, Ech: Echinoderm, G: Gastropod. *2 columns*  
1175 *fitting image*

1176

1177 **Table 1:** Table of facies recognized within tidal bars

1178

1179 **Table 2:** Table of data with mean values per facies and per tidal bars. Clay minerals semi  
1180 quantification was only realized on samples analyzed through XRD (first column of clay  
1181 fraction), but the real clay fraction for each facies was determined on more samples (second  
1182 column of clay fraction).

1183

1184

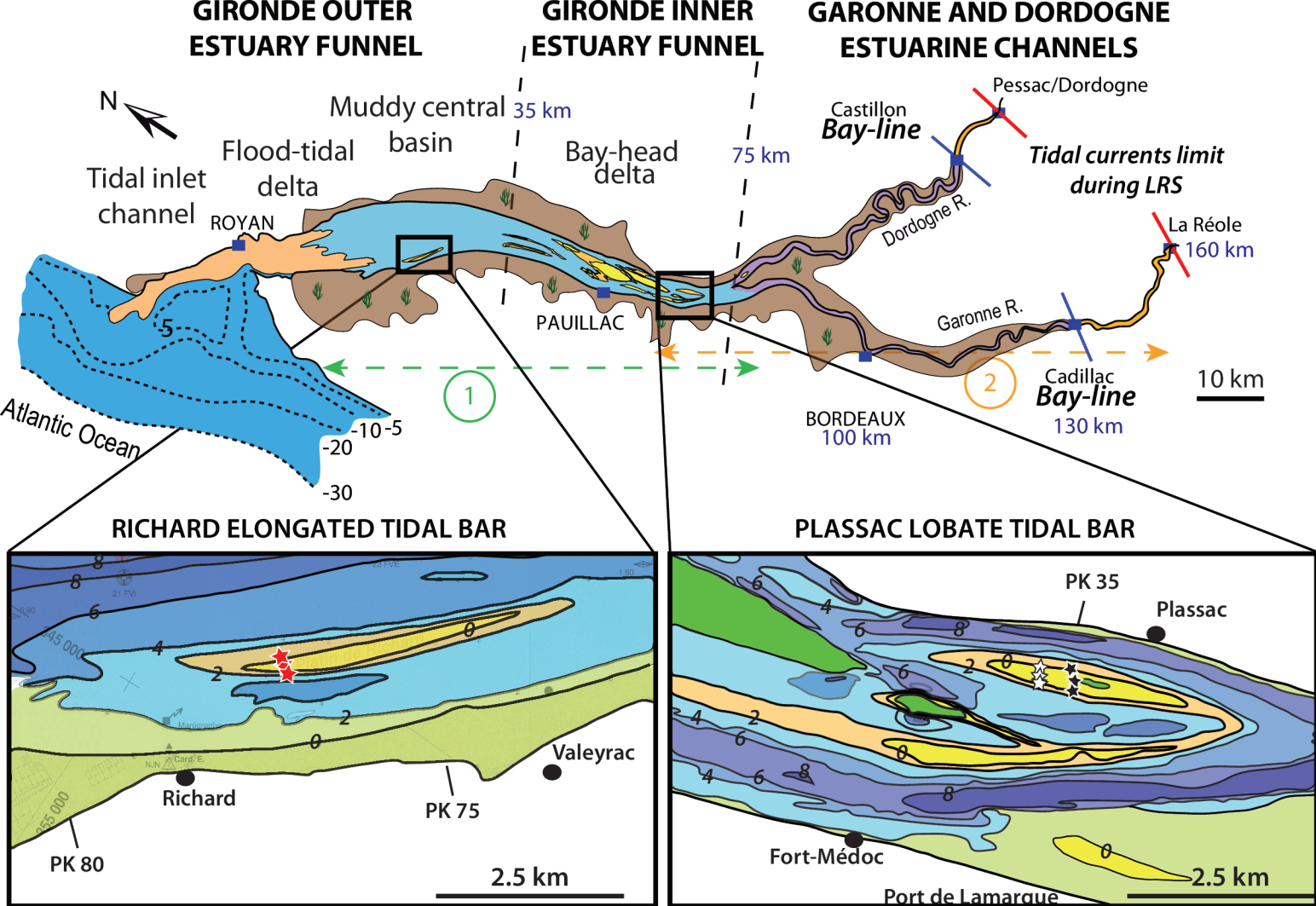
1185 **Supplementary material**

1186 **Appendix S1:** Detailed description of material and methods

1187 **Figure S1:** Correlation between CEC analysis and FTIR parameters (water band and  
1188 AL<sub>2</sub>OH+2253 nm adsorption bands)

1189 **Appendix S2:** Data table per tidal bar showing results from semi-quantifications on thin  
1190 sections.

1191



**LEGEND :**

- Fluvial-estuarine transition point bars
- Estuarine heterolithic point bars
- Tidal mudflats and marshes
- Estuary funnel tidal bars
- Estuarine mud
- Tidal inlet channel fill

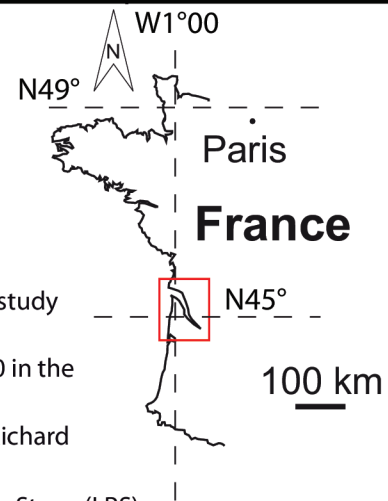
- Tidal bars supratidal zone
- Tidal bars intertidal zone
- Tidal bars subtidal zone
- Bathymetric lines

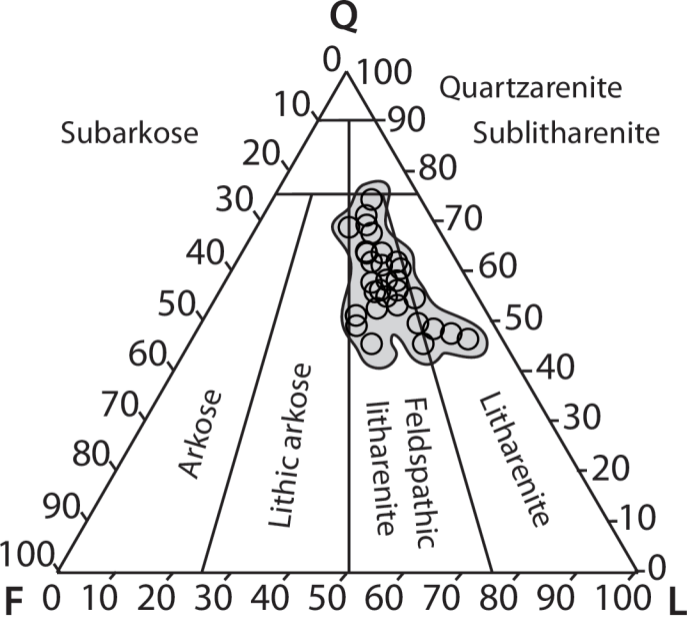
- Cores location realized in this study in the Plassac tidal bar
- Cores location realized in 2010 in the Plassac tidal bar
- Core transect location in the Richard tidal bar

XX km: Distance from the estuary mouth

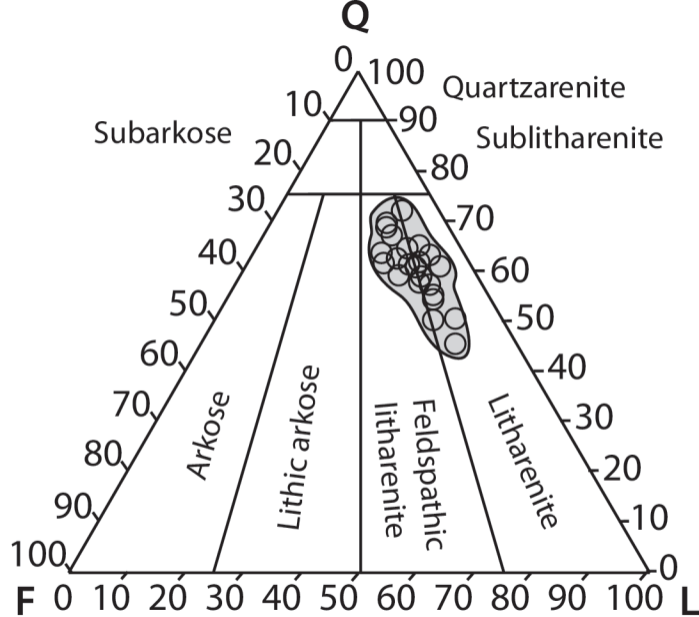
← - - - → TMZ position during High-River Stage (HRS)

← - - - → TMZ position during Low-River Stage (LRS)



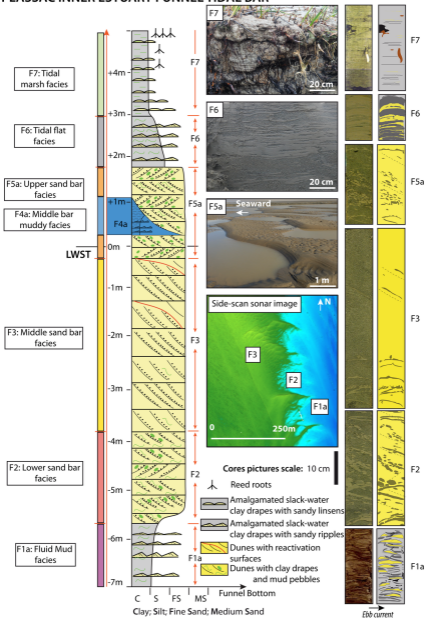


Plassac cores

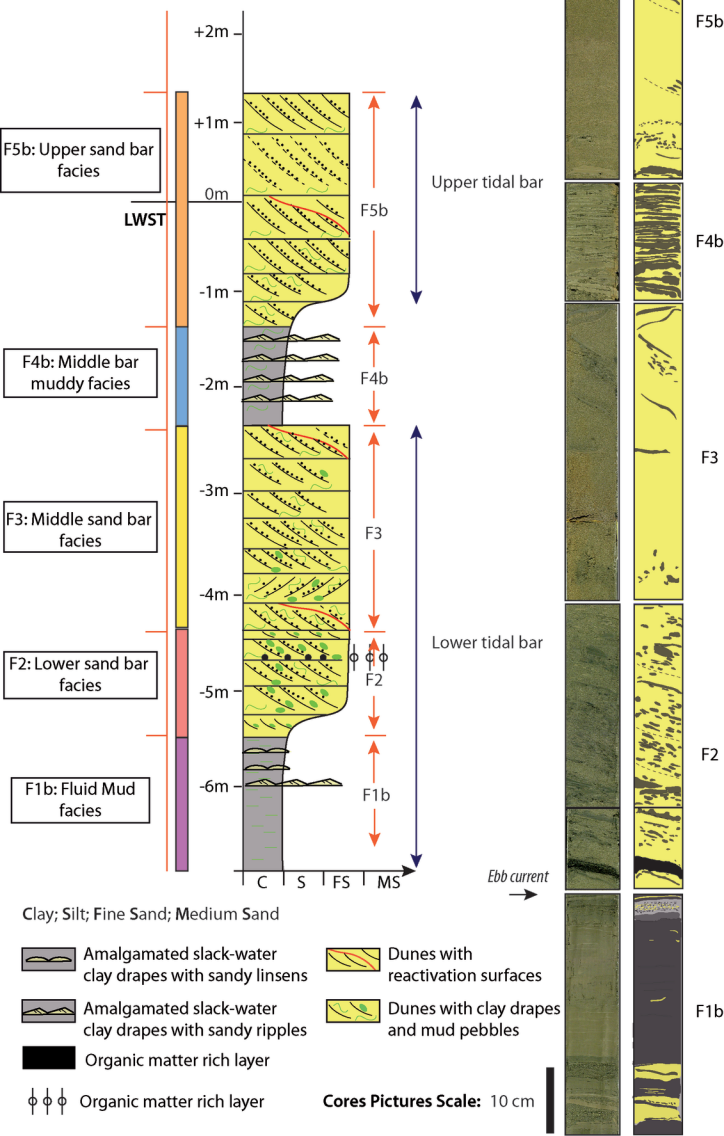


Richard cores

# PLASSAC INNER ESTUARY FUNNEL TIDAL BAR

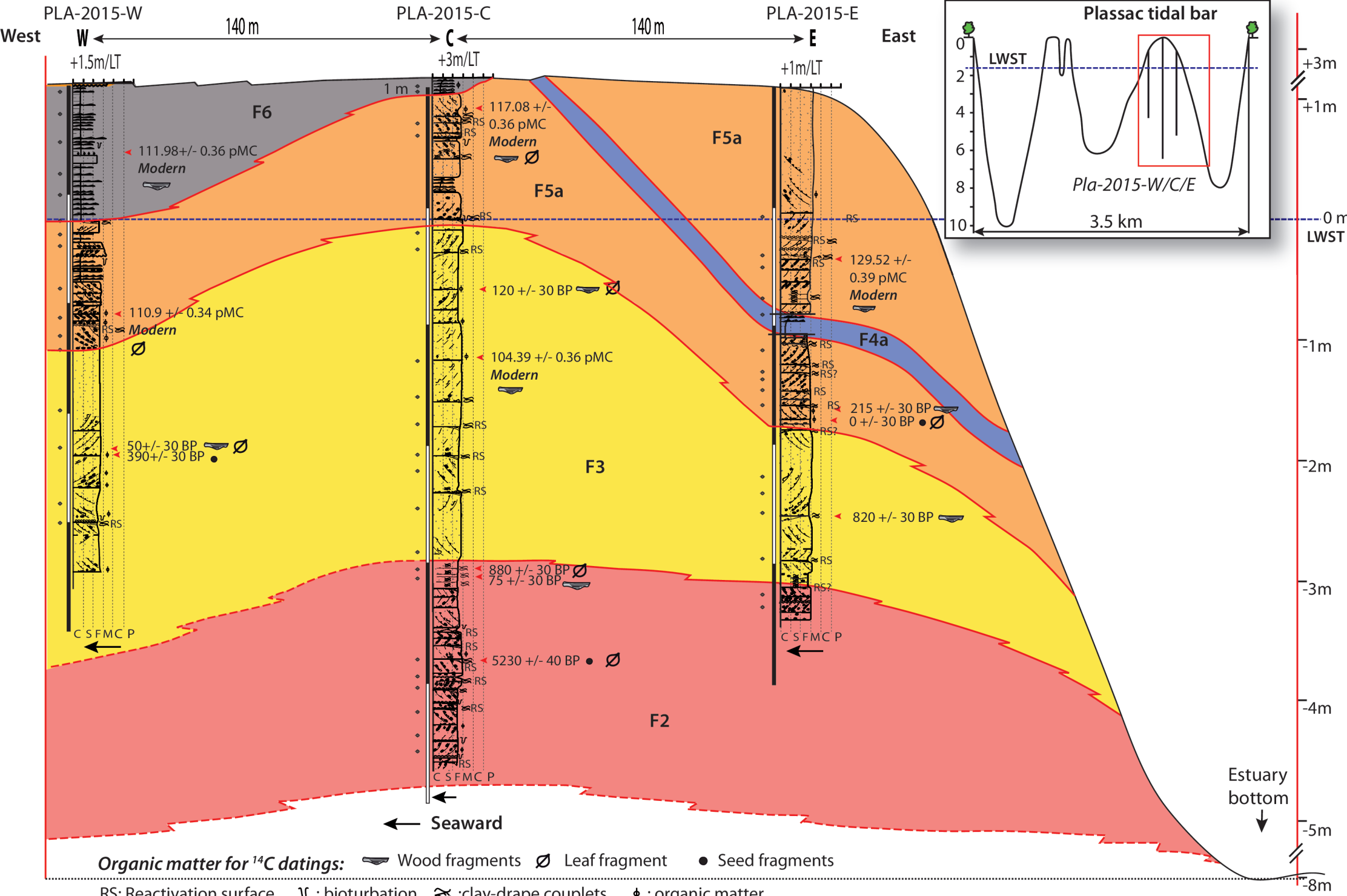


# RICHARD OUTER ESTUARY FUNNEL TIDAL BAR





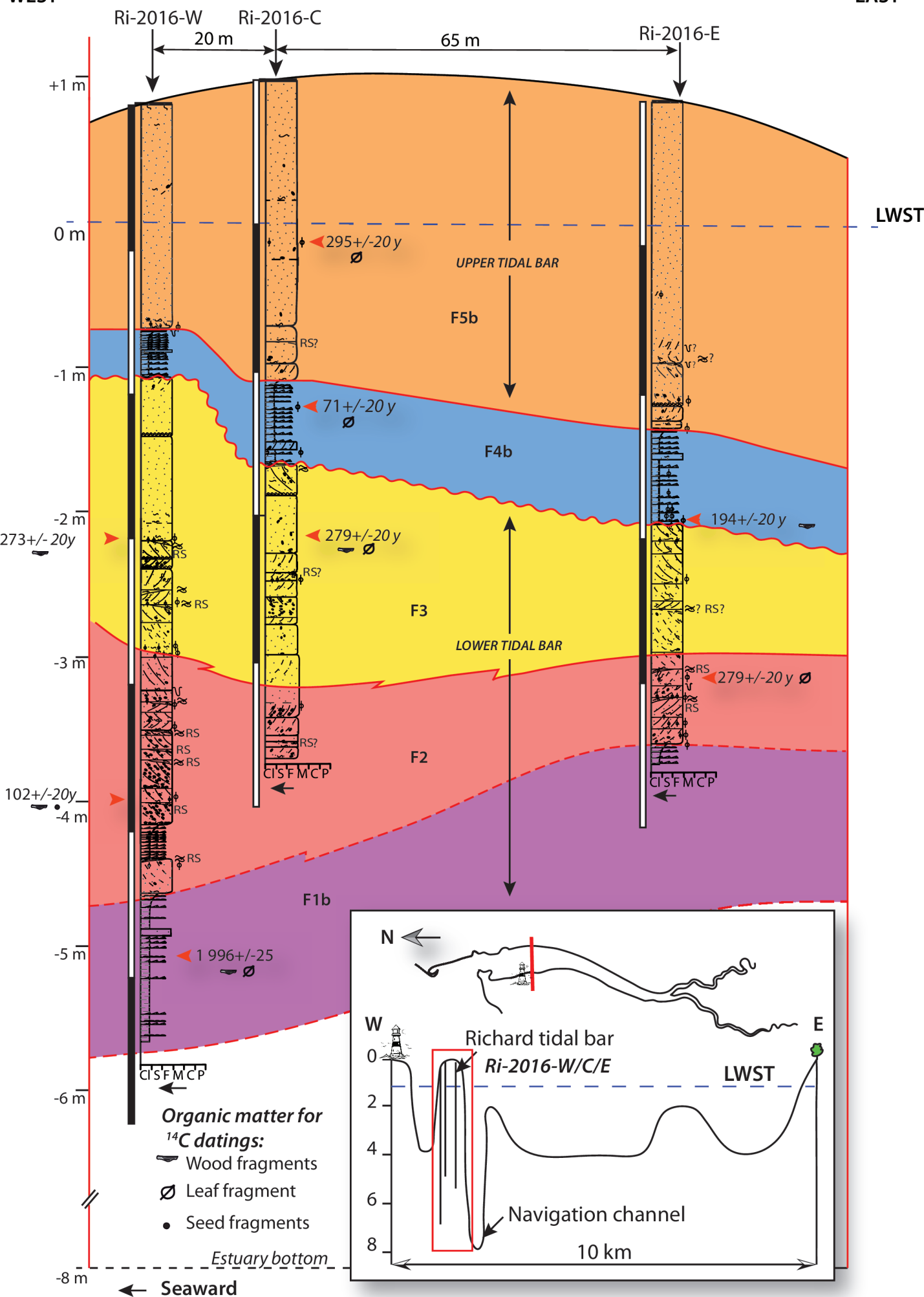
# Plassac tidal bar cross-section

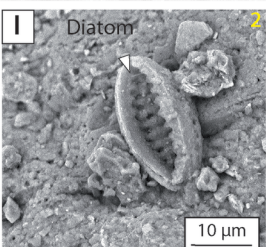
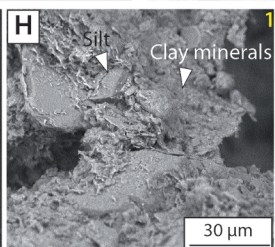
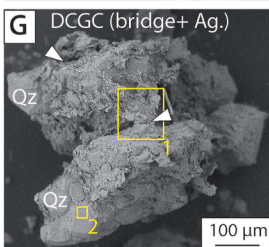
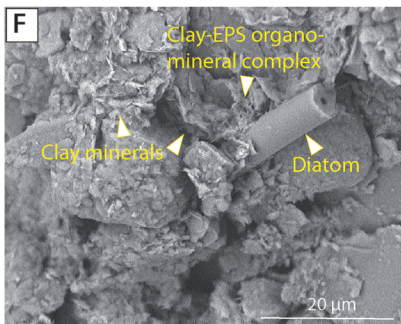
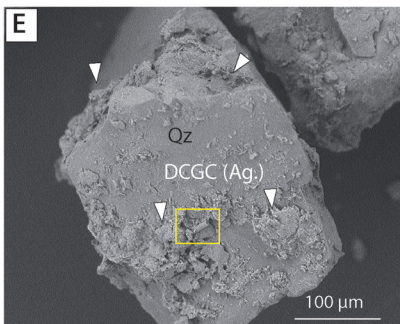
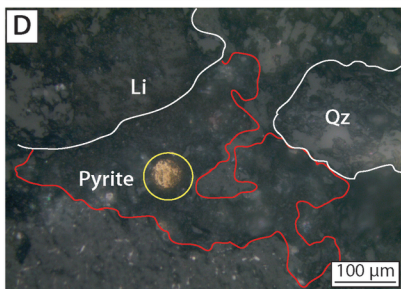
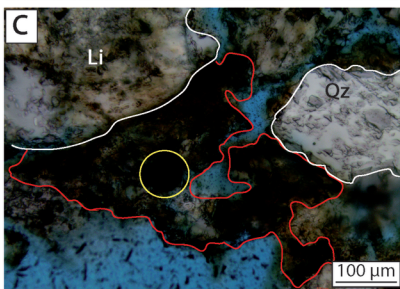
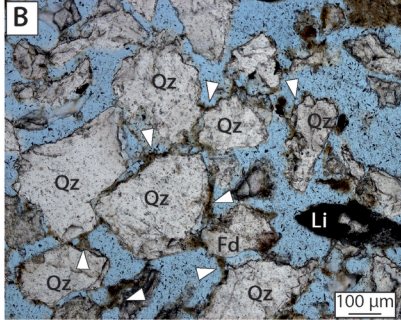
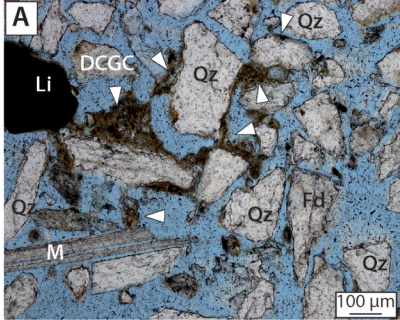


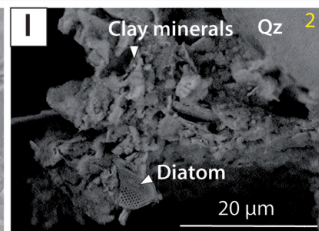
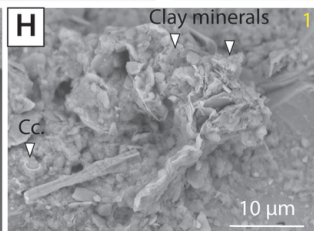
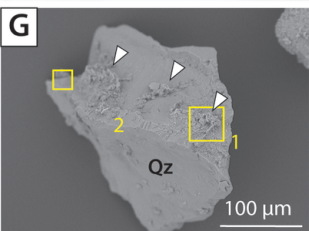
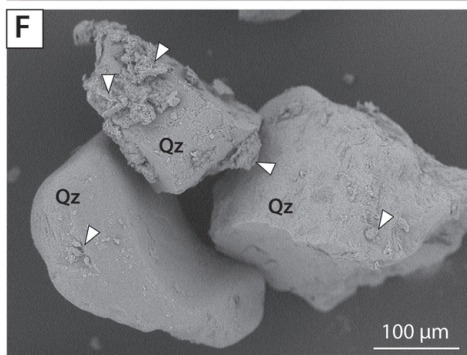
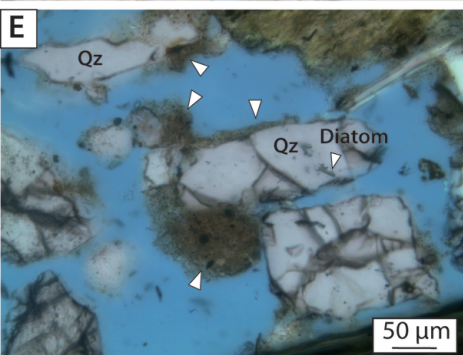
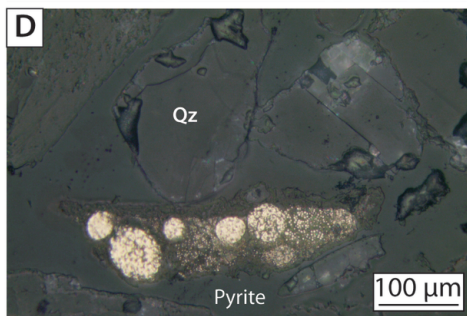
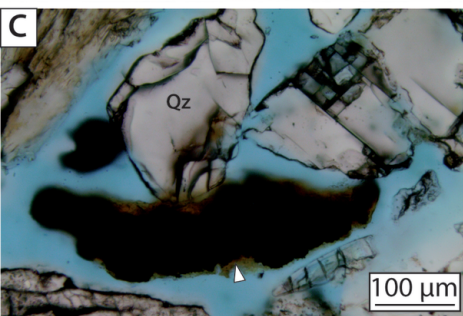
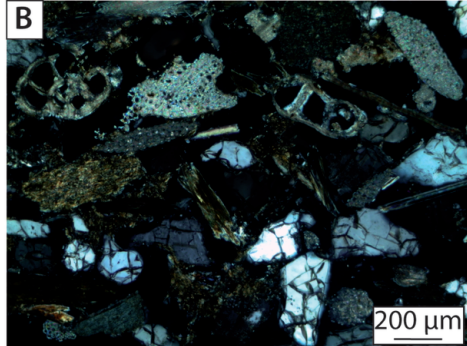
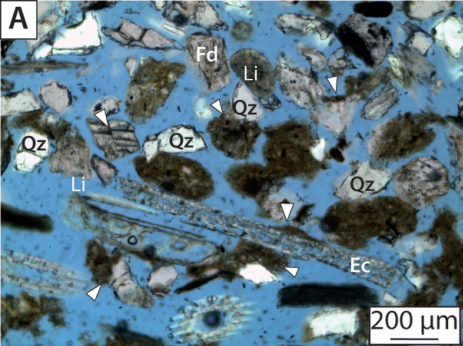
# Richard tidal bar cross-section

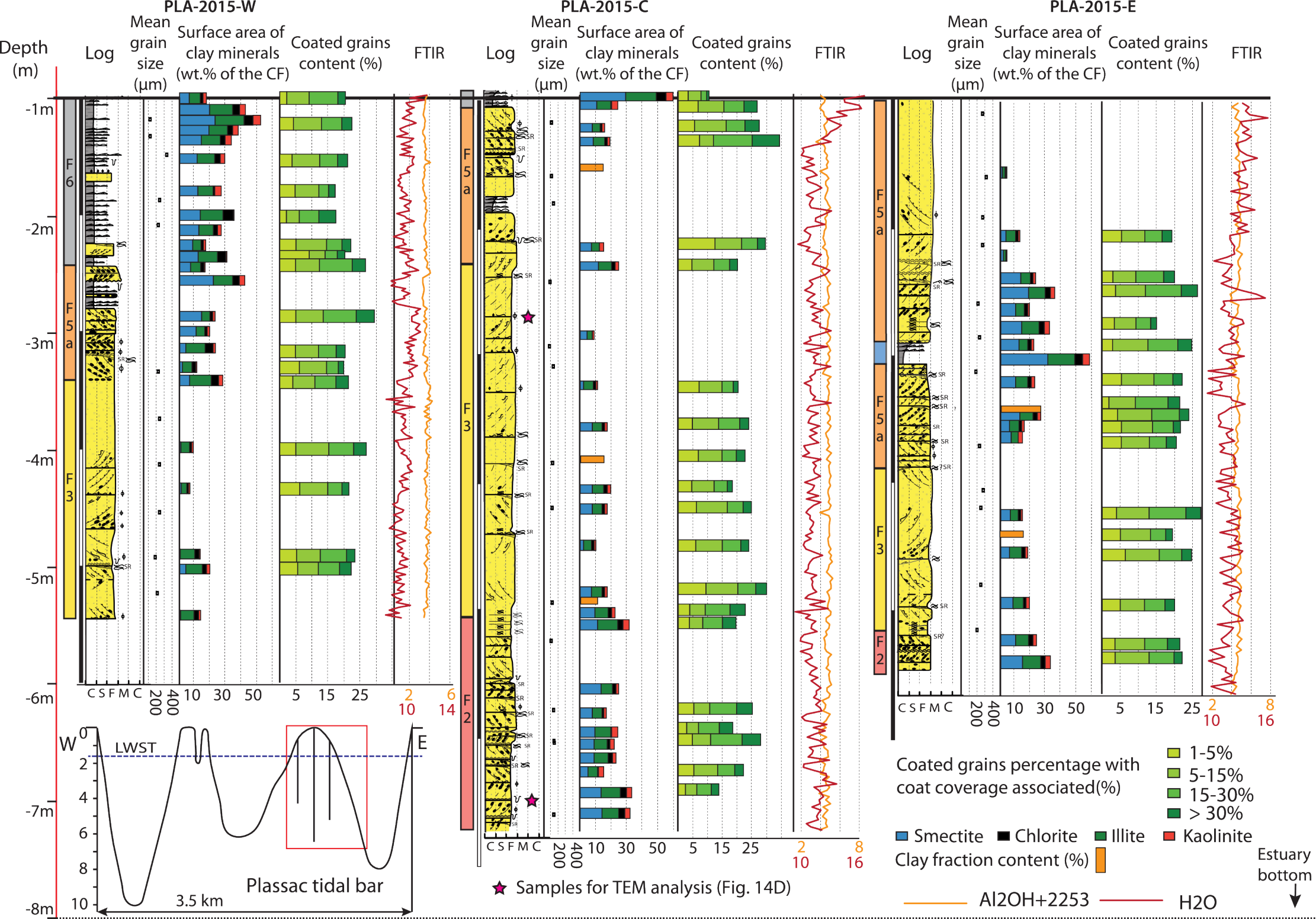
WEST

EAST





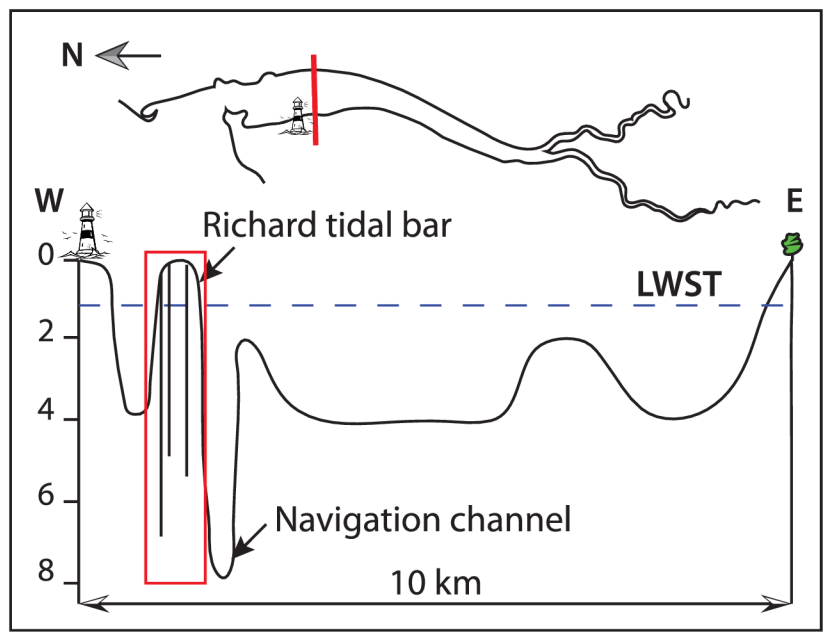
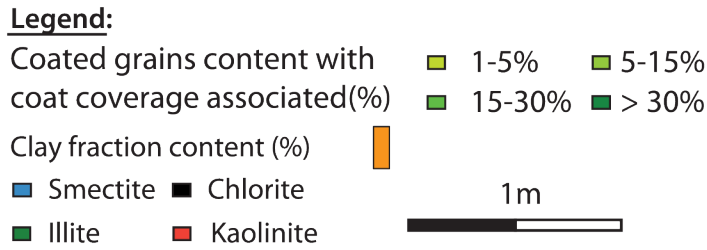
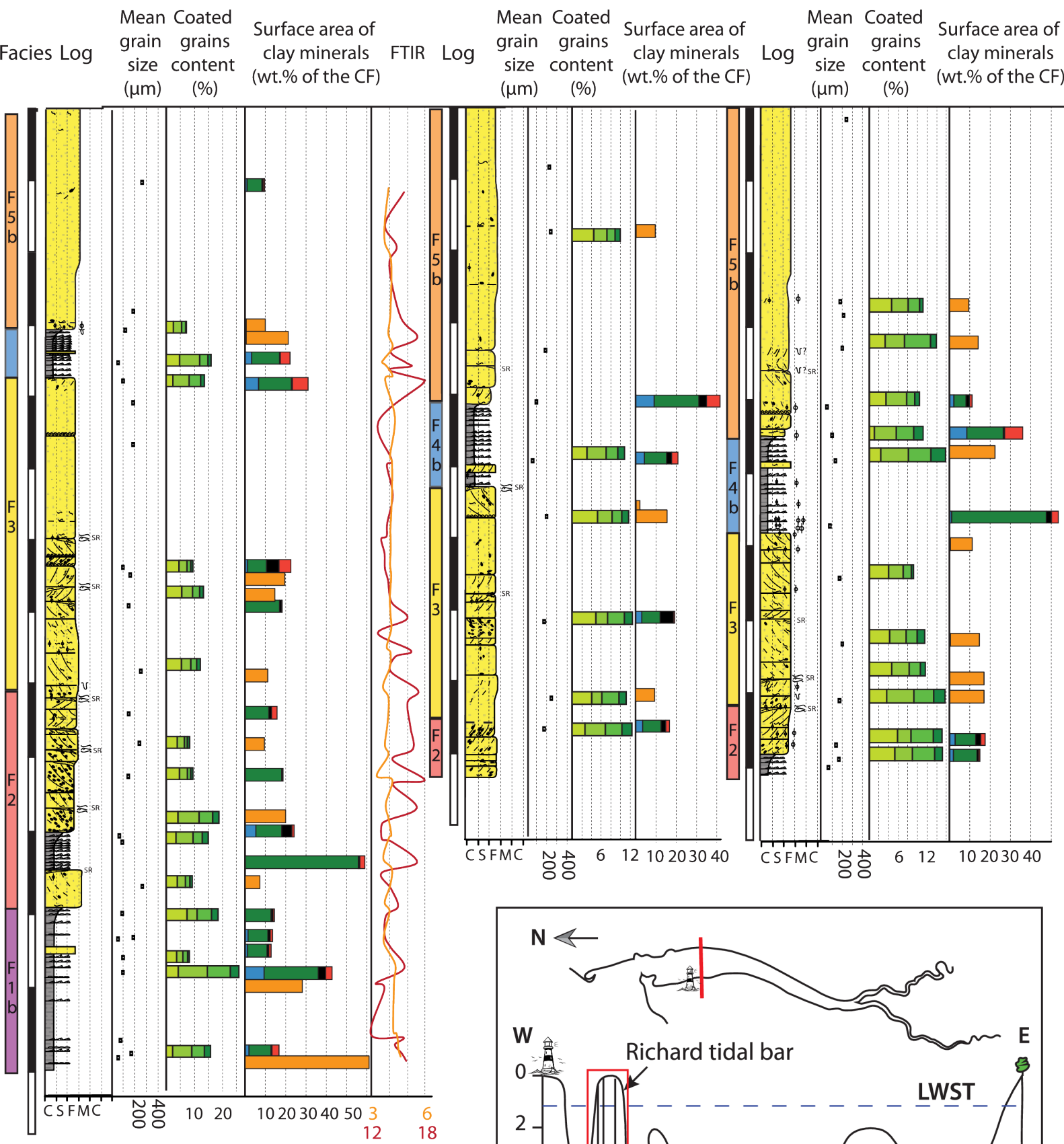




Ri-2016-W (6.5m)

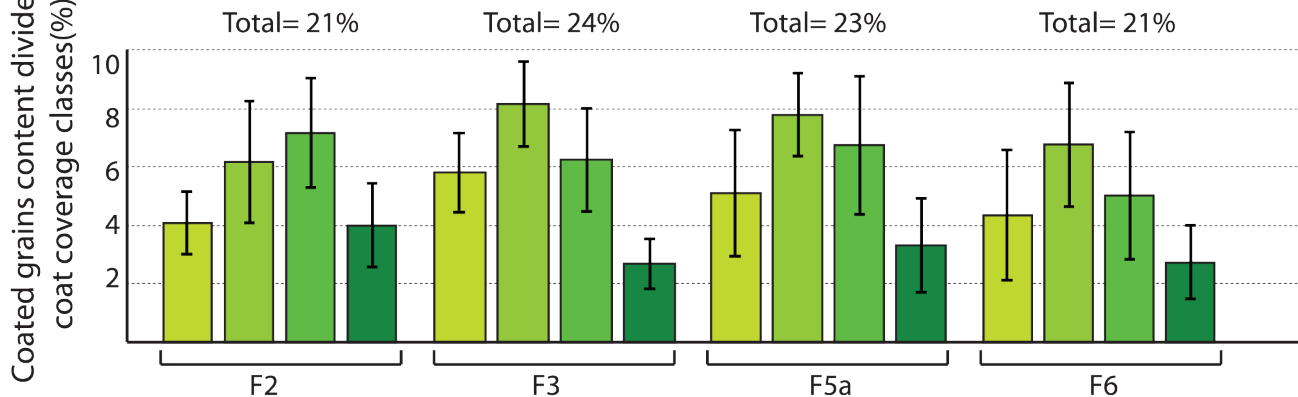
Ri-2016-C (4.6m)

Ri-2016-E (4.6m)

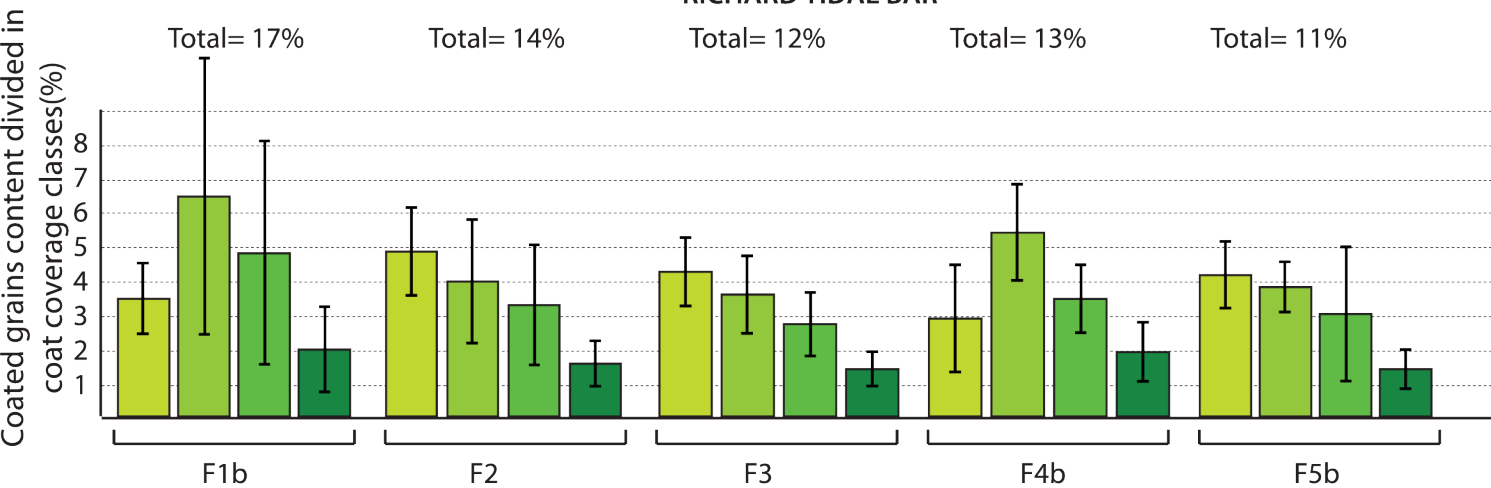


— Al<sub>2</sub>O<sub>3</sub>+2253 — H<sub>2</sub>O

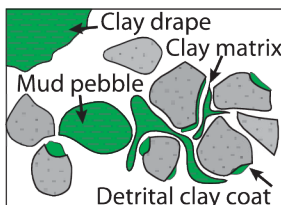
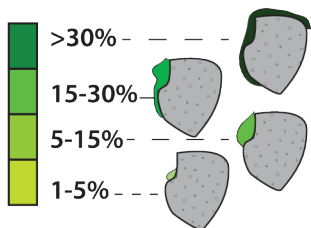
### PLASSAC TIDAL BAR



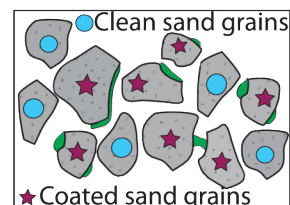
### RICHARD TIDAL BAR



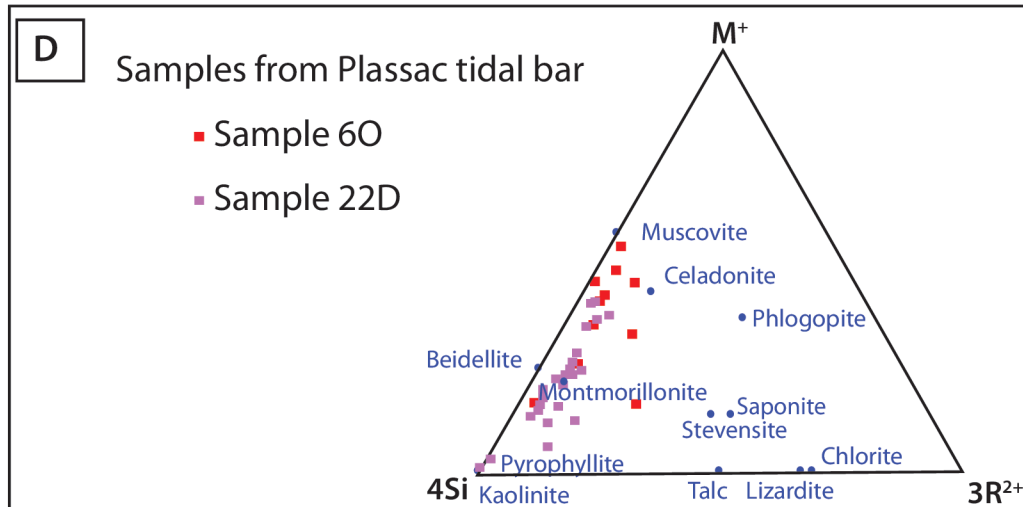
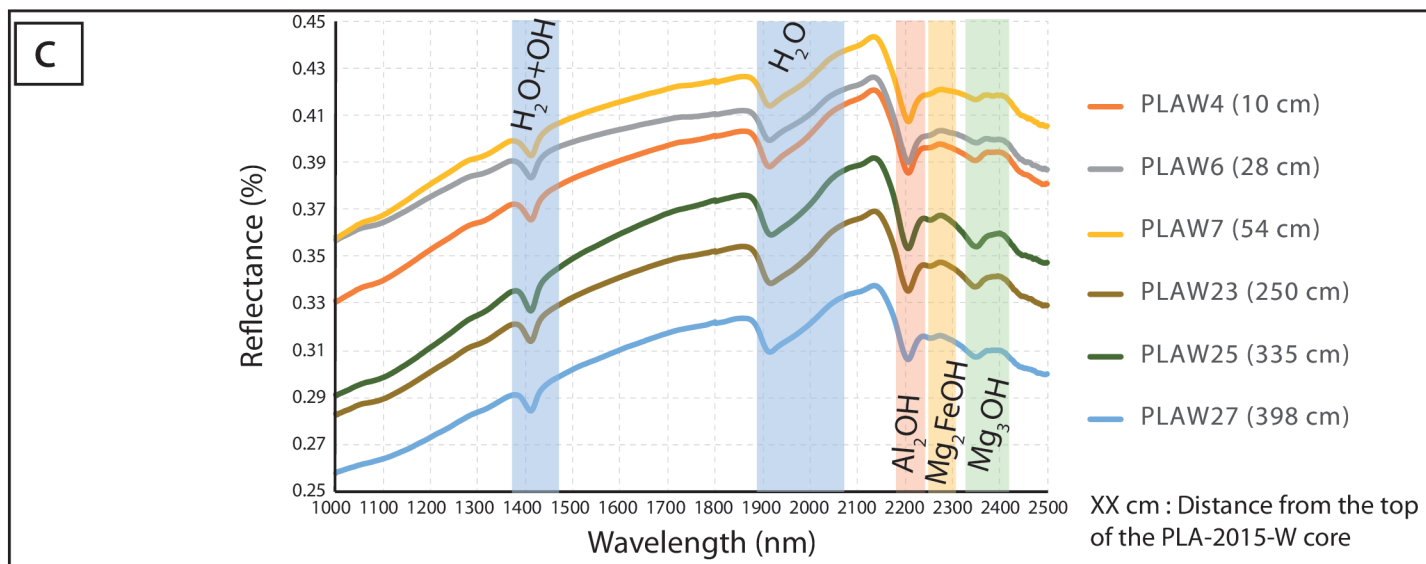
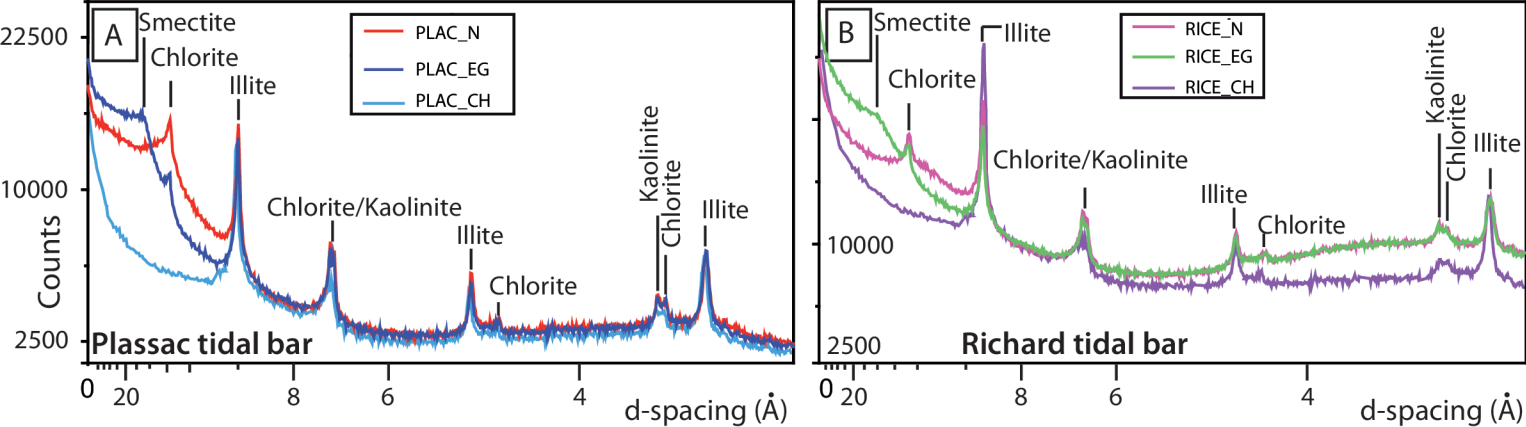
#### Legend:



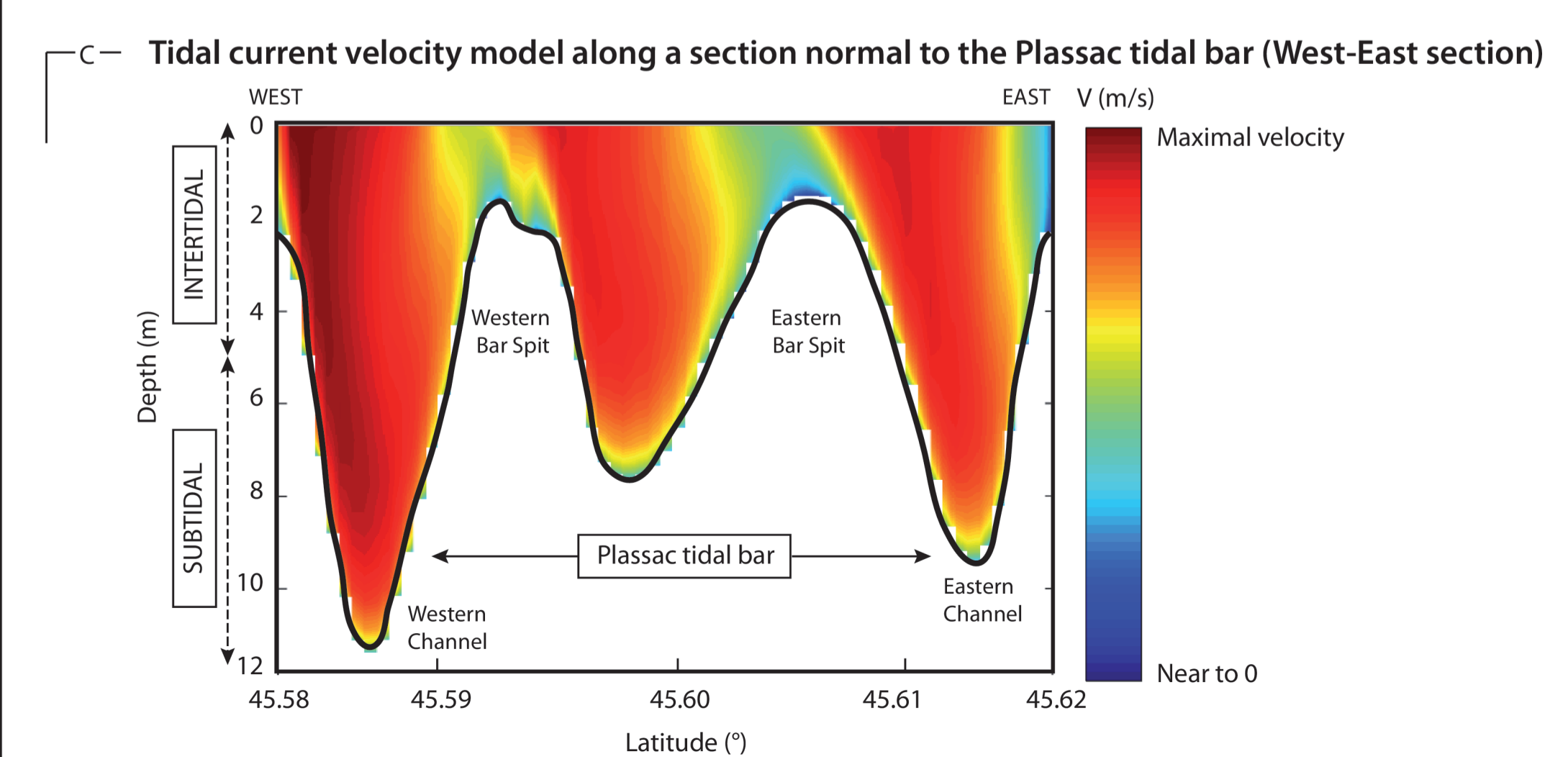
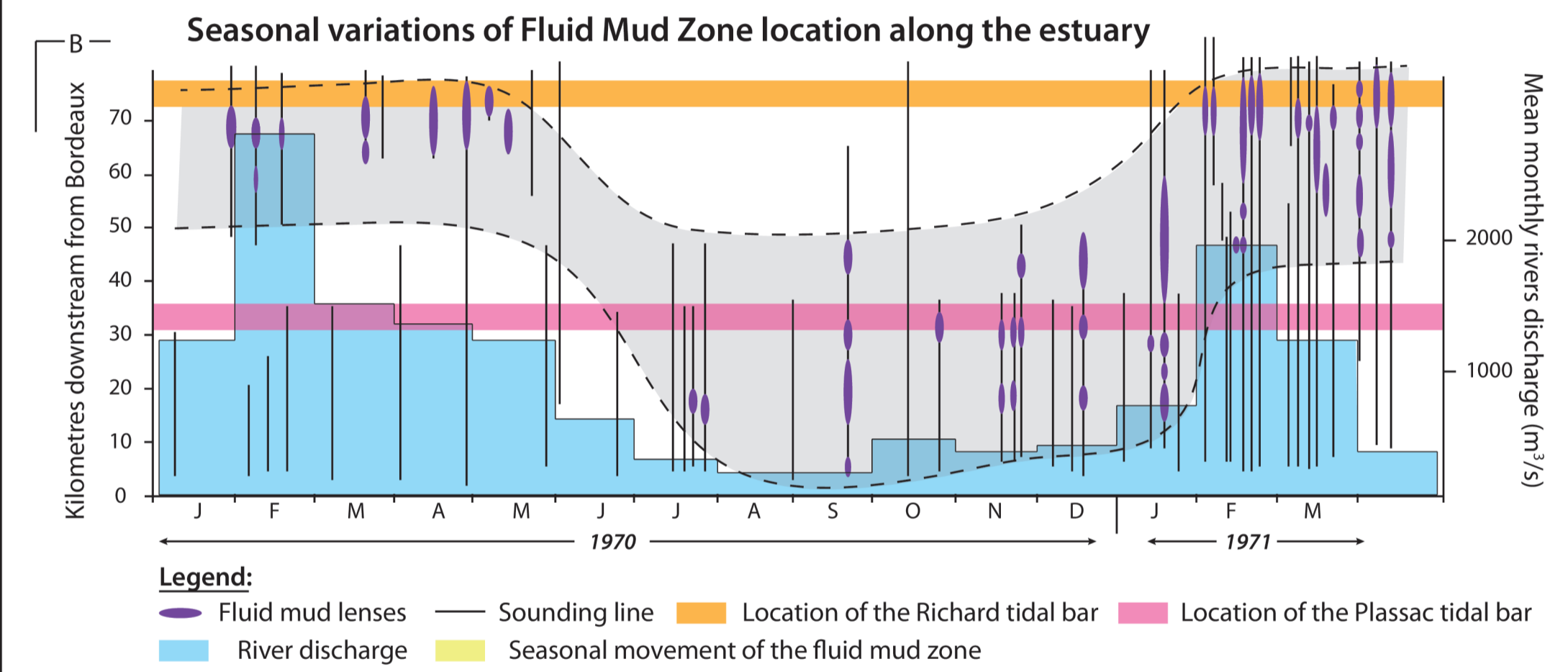
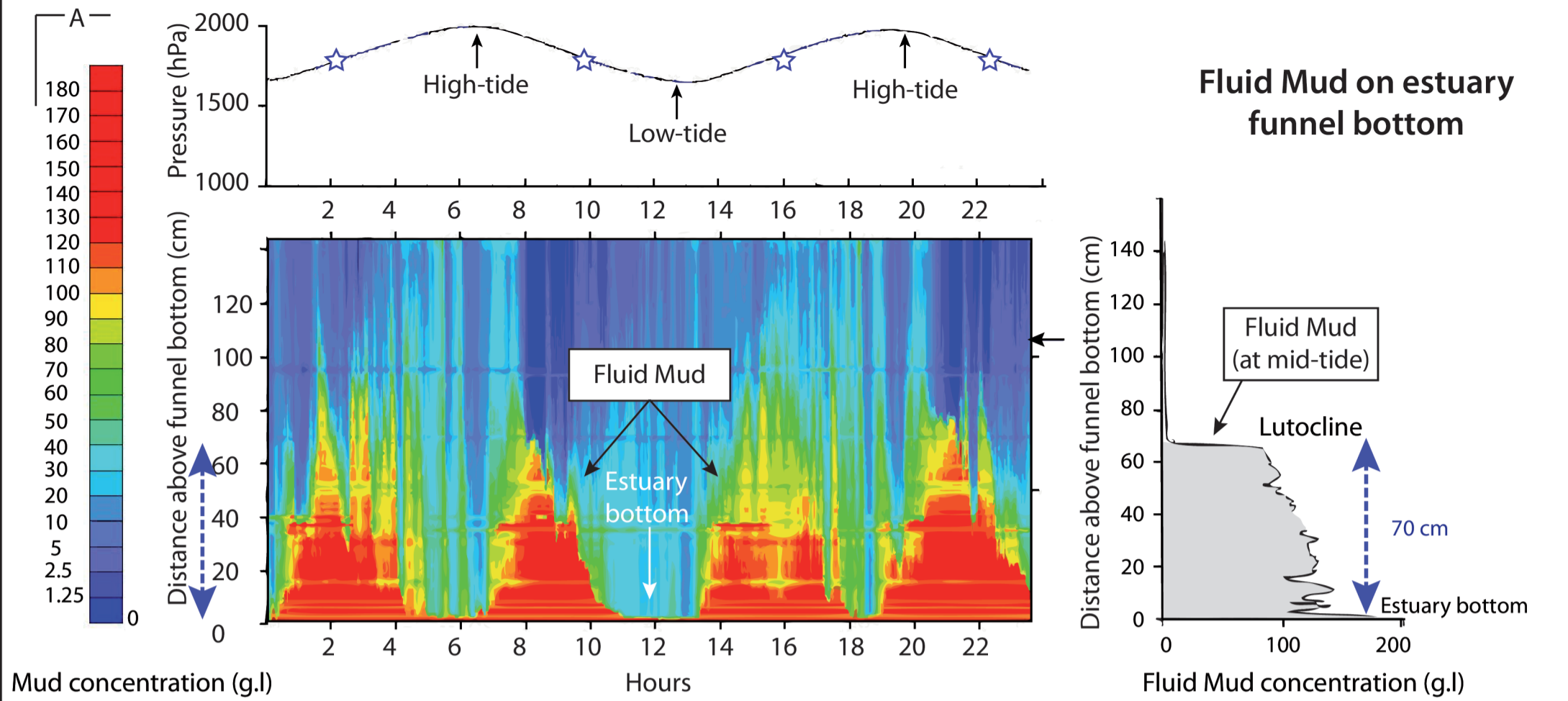
Origin of clay fraction  
(■)



% Coated grains =  $\frac{\text{Number of coated grains} \star}{\text{Total grains} \bullet + \star}$

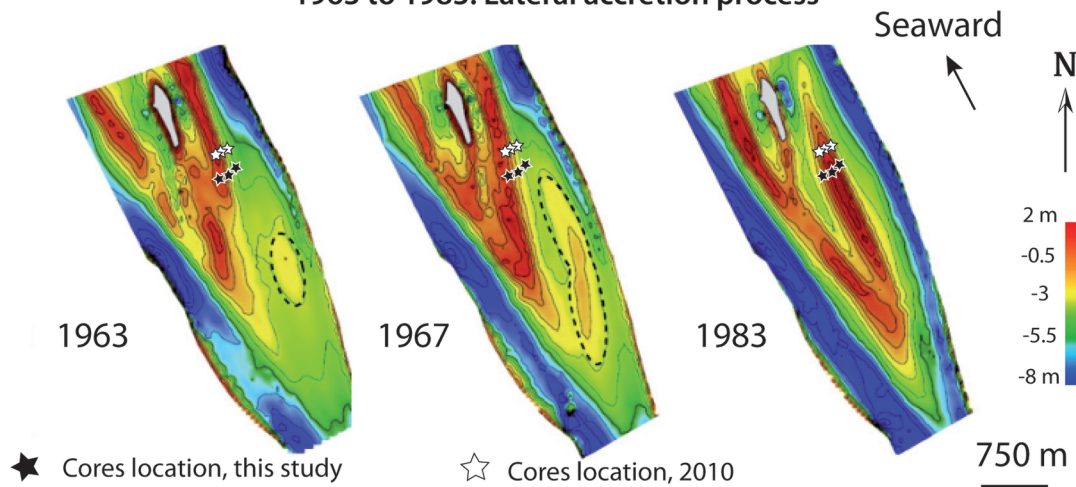






**Morphological evolution of the Plassac tidal bar from 1963 to 1983: Lateral accretion process**

A



B

**Morphological evolution of the Richard tidal bar from 1901 to 1996: combination of longitudinal and lateral accretion processes**

Bathymetric line (-2m)

— 1901

— 1948

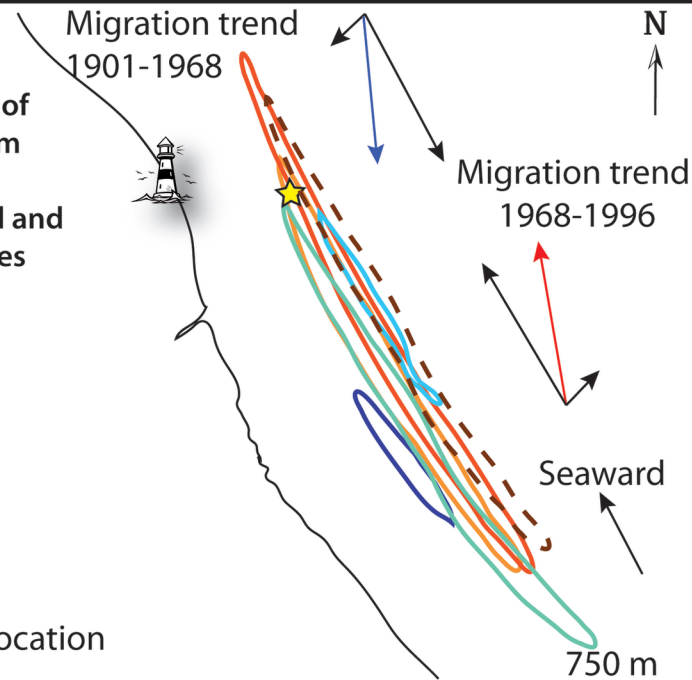
— 1968

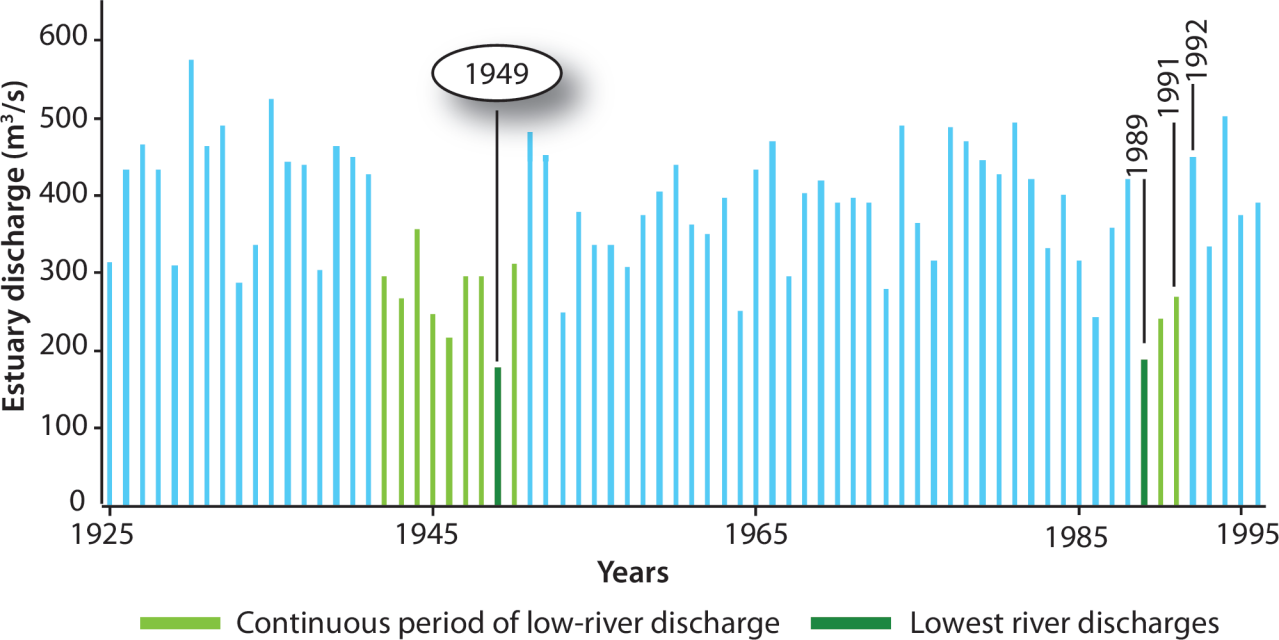
— 1984

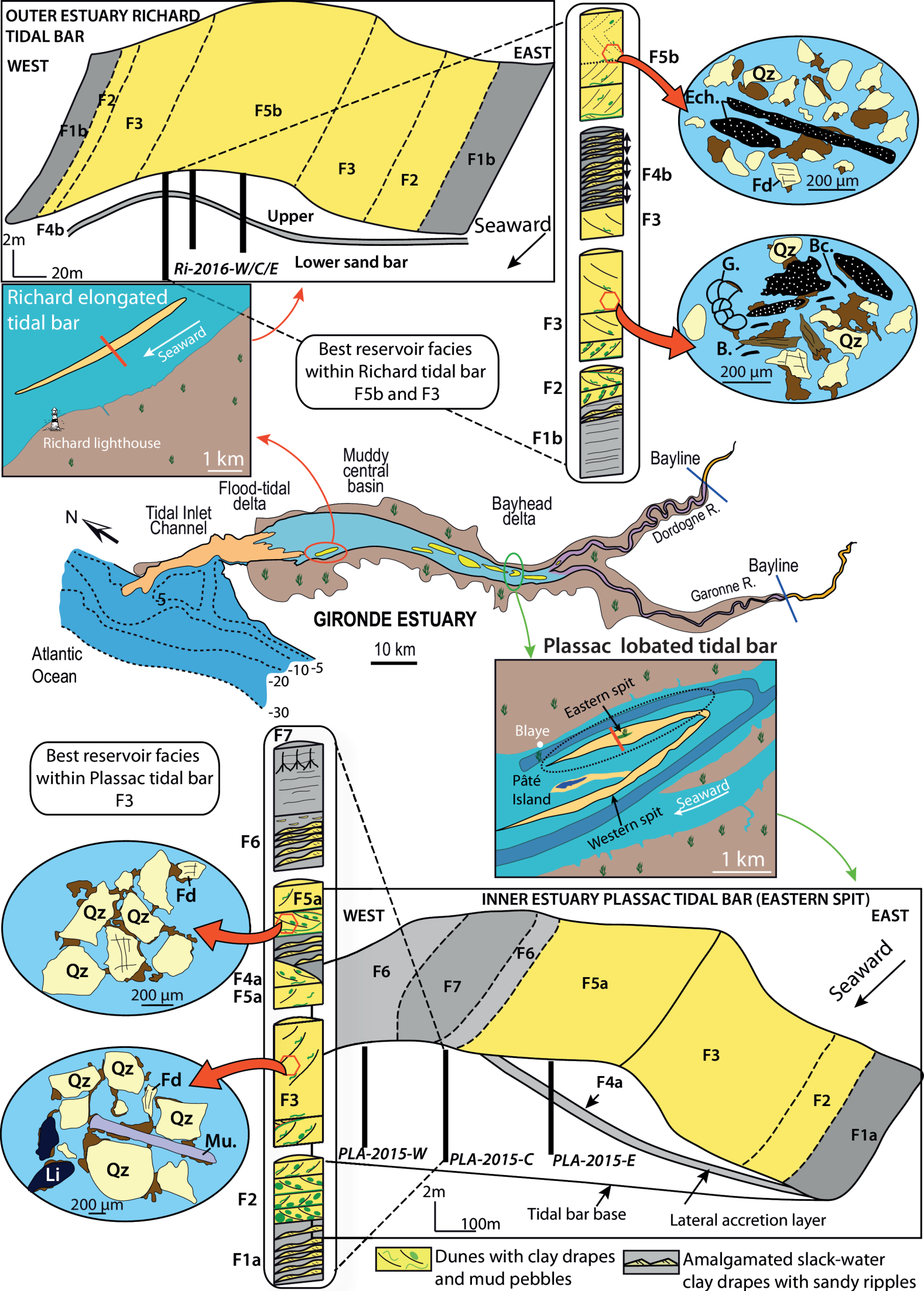
— 1996

- - Present day

★ Core transect location







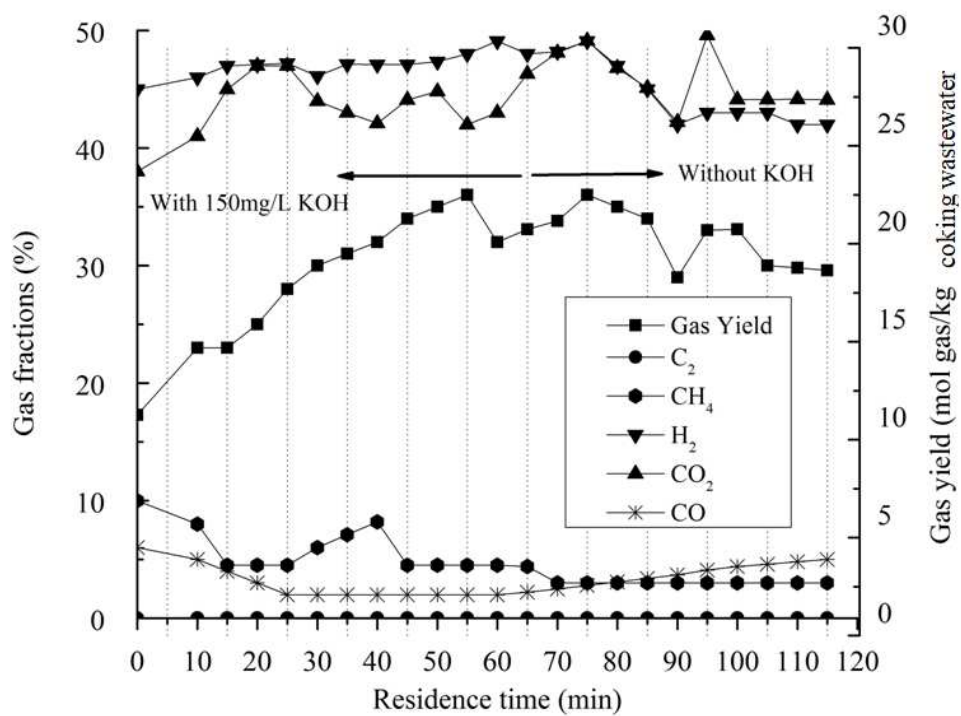


**Fig.4** The composition and total yield of the gas product from SCWG of coking wastewater with 150 mg/L KOH and without KOH (540°C, 25 MPa).

	Facies number	Coated grain content divided according to the different coat						Porosity (%)	Mean grain size (µm)	Clay minerals (reduced to the percentage of clay)					Clay fraction (wt%) from XRD samples	Total clay fraction (all samples) (wt%)
		Number of samples	1-5%	5-15%	15-30%	> 30%	Total coated grain content			Number of samples	Smectite	Illite	Chlorite	Kaolinite		
Plassac tidal bar	F6	8	4	7	5	3	19	25	208	12	15	12	4	3	34	34
	F5a	20	5	8	7	4	24	25	237	25	9	7	2	2	20	20
	F4a	/	/	/	/	/	/	/	/	1	31	17	5	5	58	58
	F3	16	6	8	6	3	23	26	224	20	5	7	2	2	15	15
	F2	8	4	6	7	4	21	25	231	12	11	9	2	3	26	25
Average Plassac		<b>Σ=52</b>	<b>5</b>	<b>7</b>	<b>6</b>	<b>3</b>	<b>22</b>	<b>25</b>	<b>225</b>	<b>Σ=70</b>	<b>14</b>	<b>11</b>	<b>3</b>	<b>3</b>	<b>31</b>	<b>30</b>
Richard tidal bar	F5b	5	4	3	3	1	11	35	178	10	3	10	1	3	17	17
	F4b	4	3	5	3	2	13	33	99	4	5	23	2	5	35	37
	F3	12	4	4	3	1	12	38	182	12	3	13	4	4	23	14
	F2	8	5	4	3	2	14	34	166	10	2	20	2	2	25	21
	F1b	3	3	6	5	2	17	31	138	6	4	14	2	2	21	29
Average Richard		<b>Σ=32</b>	<b>4</b>	<b>5</b>	<b>3</b>	<b>2</b>	<b>13</b>	<b>34</b>	<b>153</b>	<b>Σ=42</b>	<b>3</b>	<b>16</b>	<b>2</b>	<b>3</b>	<b>24</b>	<b>24</b>